COMPARISONS OF BRDF THEORIES WITH EXPERIMENT

by

YauJen Wang

A Dissertation Submitted to the Faculty of the

COMMITTEE ON OPTICAL SCIENCES (GRADUATE)

In Partial Fulfillment of the Requirements
For the Degree of

DOCTOR OF PHILOSOPHY

In the Graduate College

THE UNIVERSITY OF ARIZONA

1 9 8 3

THE UNIVERSITY OF ARIZONA
GRADUATE COLLEGE

As members of the Final Examination Committee, we certify that we have read the dissertation prepared by YAUJEN WANG

entitled Comparisons of BRDF Theories with Experiment

and recommend that it be accepted as fulfilling the dissertation requirement for the Degree of Doctor of Philosophy.

D. Sewell	Feb 22 83
	Date
M. Sargent III	Feb 23, 83
	Date
W. Wolfe	2/23/83
	Date
	Date
	Date

Final approval and acceptance of this dissertation is contingent upon the candidate's submission of the final copy of the dissertation to the Graduate College.

I hereby certify that I have read this dissertation prepared under my direction and recommend that it be accepted as fulfilling the dissertation requirement.

William L Wolfe	3/4/83
Dissertation Director	Date

STATEMENT BY AUTHOR

This dissertation has been submitted in partial fulfillment of requirements for an advanced degree at The University of Arizona and is deposited in the University Library to be made available to borrowers under rules of the Library.

Brief quotations from this dissertation are allowable without special permission, provided that accurate acknowledgment of source is made. Requests for permission for extended quotation from or reproduction of this manuscript in whole or in part may be granted by the copyright holder.

SIGNED: 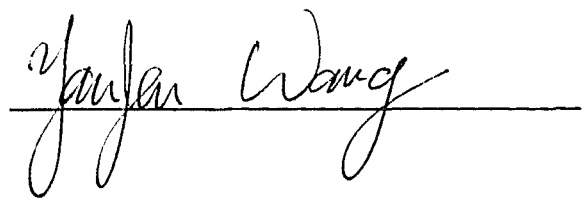

To my parents and my brothers and sister

ACKNOWLEDGMENTS

I gratefully acknowledge the supervision, assistance, discipline, and encouragement of my advisor, Professor William L. Wolfe, during their graduate program. I am also grateful to members of my committee, Professor Murray Sargent III and Professor Dror Sarid, for their valuable comments and assistance.

I have also benefited from discussions with my colleagues, Mr. Langford G. Brod and Dr. Frederick O. Bartell. Profound appreciation is due to Dr. Larry L. Brooks for his guidance in experimentation and to Mr. John Hubbs for valuable assistance in data reduction.

I would also like to express appreciation to Dr. Jean Bennett of the Naval Weapons Center, China Lake, California, for her measurements and cooperation; to Professor James C. Wyant of the Optical Sciences Center for his measurements; and to Dr. Eugene Church of the Army Armament Research and Development Command for his valuable comments.

I wish to express my sincere appreciation to Ms. Kathleen Seeley and Ms. Martha Stockton for their typing and editing.

This research program was carried out with financial support from the U.S. Air Force under contract F49620-80-C-0022.

TABLE OF CONTENTS

TABLE OF CONTENTS--Continued

LIST OF TABLES

LIST OF ILLUSTRATIONS

ABSTRACT

Scalar and vector electromagnetic boundary-value theories of surface scattering have been applied to a microrough sample of fused silica coated with aluminum. Surface profiles were made with a mechanical and interferometric profilometer. The resulting values of rms surface height and autocorrelation length were used to calculate the scattering for various angles, wavelengths, and polarization conditions. Bidirectional reflectance distribution function (BRDF) measurements associated with scatter value were made and their corresponding power spectra were generated. Both were used to compare with the theoretical values. Special attention was also paid to the various methods of determining optical parameters with the BRDF data and the corresponding power spectra.

CHAPTER 1

INTRODUCTION

Scattering from almost-smooth surfaces grows increasingly important as optical systems become more sophisticated. Recently, considerable attention has been paid to scattering problems in high-power lasers, large earth (space) telescopes, x-ray telescopes, laser gyro systems, missile systems, and high-quality optical systems. For more than two decades the study of scattering from rough surfaces has been carried out partly to understand and overcome unwanted stray light.

Two major theories, scalar and vector, have been widely applied to investigate these problems. Calculations of the amount and distribution of scattering have been made for sound, radar, infrared radiation, and visible light from rough surfaces such as terrain, the sea, and optical surfaces. Scalar theory based on a scalar diffraction integral has been developed by Davies (1954), Beckmann and Spizzichino (1963), Harvey (1976), and Chandley and Welford (1975). Vector theory based on a perturbation technique for solving boundary value problems was originated by Rayleigh (1945), extended by Rice (1951), and developed more recently by a number of authors (Church, Jenkinson, and Zavada, 1977; Elson and Bennett, 1979b; Marvin, Toigo, and Celli, 1975; Maradudin and Mills, 1975; Barrick and Peake, 1967; Ishimaru, 1978; and Kroger and Kretschmann, 1970).

Extensive experimental data on surface-roughness scattering of smooth mirrors as well as diamond-turned surfaces as a function of angles of incidence and angles of scattering in the visible region are available in the literature (Beaglehole and Hunderi, 1970; Elson and Bennett, 1979a; Church et al., 1977; Noll and Glenn, 1982; Eastman and Baumeister, 1974; Chandley, 1976; and Bennett, 1976). Some authors have also used two wavelengths (Young, 1975) or several wavelengths (Wang and Wolfe, 1983) to enlarge the spectral range of their scattering studies. However, there seems to have been no systematic comparison of the various theories and data.

Questions relating to the variation of scattering with angle of incidence and the relationship between scattering and wavelength remain unanswered. Can we effectively explain or predict the bidirectional reflectance distribution function (BRDF) (Nicodemus, 1970) with a reliable theory, either scalar or vector, or both? Furthermore, how do these two theories compare with experimental data?

It is well understood that one of the assumptions of classical scalar diffraction theory of scattering from surfaces is that the light is not polarized and the surface autocorrelation function is Gaussian (Beckmann and Spizzichino, 1963; Davies, 1954). Unfortunately, the Gaussian autocovariance function does not agree with most measurements (Eastman and Baumeister, 1974; Bennett, 1976; and Chandley, 1976) and modern optical instruments are not necessarily unpolarized. Can scalar theory be modified to agree with data? What and how drastic must these modifications be?

This dissertation attempts to answer the questions posed above by comparing these two theories using two different approaches. The first approach is a straightforward comparison between BRDF data and each proposed theory. The second approach is a comparison of the power spectra of the surface height distribution calculated with different theories from multiple-wavelength data.

The description of BRDF expressions is given in Chapter 2. The optical factor of vector theory generally is a complex function consisting of several optical parameters. In this dissertation, the optical factors will be simplified according to the direction of polarization, the orientation of the measurement, the sample material, and the spectral range used. We will rederive and compare those optical factors calculated by other authors in those cases in which the incident wavelength is much larger than the rms height of rough surfaces. Scalar theory, which assumes the radiation to be unpolarized, will be applied to and compared with the polarized data which in our measurements do not show significant ellipticity.

A brief description of the scatterometer is given in Chapter 3. Attention is paid to the method of taking the BRDF measurements, i.e., the "straight-through" method. Although it requires careful calibration and alignment, it is the calibration technique that most closely resembles the measurement situation.

The results of the experiment and the power spectra are presented in Chapter 4 and are compared with vector and scalar theory for one- and two-dimensional autocorrelation functions. The direct

curve fitting of BRDF data with theories will yield a clear picture of wavelength scaling, dimensional dependence, and an appropriate model of the autocorrelation functions. The power-spectrum approach enhances the comparison dramatically based on the concepts of uniqueness and continuity.

Following the comparisons in Chapter 4, we discuss the associated rms surface height produced by each method and theory. The uniqueness and consistency of the inferred surface-height spectrum under different measurement arrangements is the criterion for differentiating between proposed theories. There has been substantial interest in using the BRDF data to determine the rms roughness and autocorrelation length (Chandley, 1976, 1979; Elson and Bennett, 1979a). Several new techniques for calculating these optical parameters are presented and discussed.

CHAPTER 2

THEORY

It has been shown (Elson and Bennett, 1979a; Church et al., 1977) that a convenient way to write the bidirectional reflectance distribution function (BRDF) (Nicodemus, 1970) is

$$\text{BRDF} = F_\lambda \cdot F_o \cdot F_s,$$

where F_λ is the wavelength factor, F_o is the optical factor, and F_s is the surface factor. The first term, F_λ, is $(2\pi/\lambda)^4$, which is the Rayleigh blue sky factor and the primary contribution of dipole radiation. The optical factor F_o is a complicated function of the optical properties of a material (complex permittivity) and its scattering geometry (polarization state, angles of incidence and reflection). The scattering geometry is shown in Fig. 2.1, where θ_i is the angle of incidence, θ_s is the angle of scattering, and ϕ is the angle of out-of-plane scatter. The surface factor is the power spectrum of the distribution of surface height, which is the same as the Fourier transform of the surface height autocorrelation function. In the past, both Gaussian and exponential models have been used for this autocorrelation function. However, the Gaussian function does not seem to fit the data. We will therefore concentrate on the exponential model.

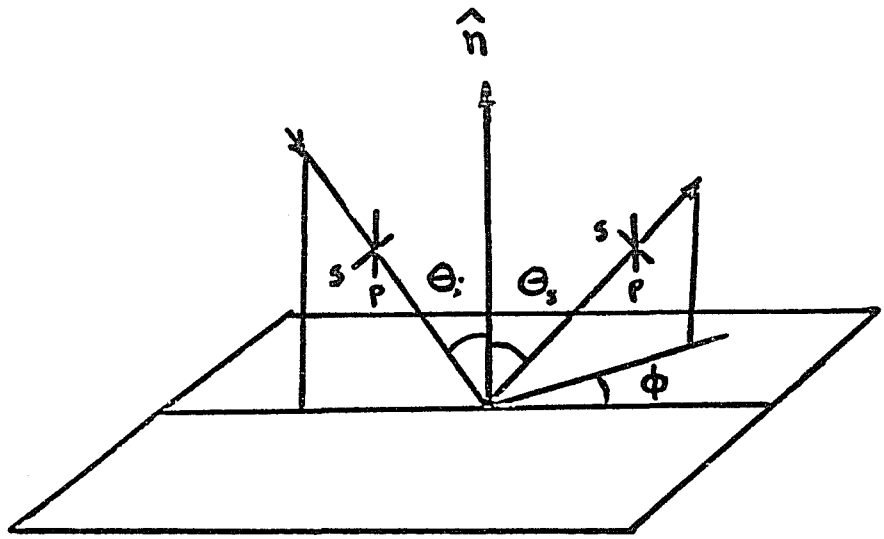

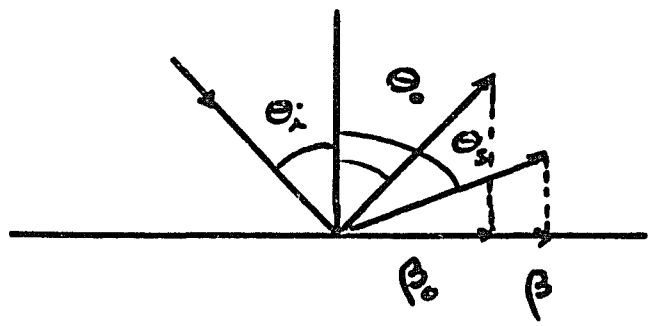

$\beta = \sin\theta_s \qquad \beta_o = \sin\theta_o$

Fig. 2.1. Geometry of Scattering.

In this chapter, the optical factors for different theories are discussed, the transition from a two-dimensional surface factor to a one-dimensional one is derived, and the relationship between an unpolarized source and an unpolarized detector (uu) and other polarized quantities is explained.

Vector Theory

Vector theory, which is a rigorous treatment of surface reflection, is based on a vector diffraction integral or a variational (perturbation) method of solving the boundary value problem of electromagnetic waves on a rough surface. The vector diffraction integral is the so-called "Stratton-Chu-Silver" integral (Silver, 1947) and was used by Leader (1971) and Fung and Chang (1969) to treat scattering from rough surfaces. The perturbation technique was first used by Rayleigh (1945), was extended by Rice (1951), and was developed more recently by a number of investigators (Elson and Bennett, 1979b; Marvin, et al., 1975; Maradudin and Mills, 1975; Barrick and Peake, 1967; Ishimaru, 1978; Kroger and Kretschmann, 1970).

The explicit general BRDF (Elson and Bennett, 1979b) for the case of incident wavelength λ much greater than the rms roughness σ can be expressed as

$$f_r \equiv \frac{1}{P}\frac{dP}{d\Omega} = \left(\frac{\omega}{c}\right)^4 \left\{\cos\theta_i \cos\theta_s \,|\, 1-\varepsilon \,|^2 \right.$$

$$\left. \times \left(\frac{|\chi\theta|^2}{|\nu_s - iq_s\varepsilon|^2} + \frac{|\chi\phi|^2}{|\nu_s - i\phi_s|^2} \right) \right\} F_s \qquad (2.1)$$

$$\chi\theta = \frac{(\nu_s \nu_i \cos\phi_s + k_s k_i \varepsilon)\cos\phi_i}{\nu_i - iq_i\varepsilon} - \frac{i(\omega/c)\nu_s \sin\phi_s \sin\phi_i}{\nu_i - iq_i}$$

and

$$\chi\phi = \frac{\omega}{c}\left(\frac{\nu_i \sin\phi_s \cos\phi_i}{\nu_i - iq_i\varepsilon} - i\,\frac{(\omega/c)\cos\phi_s \sin\phi_i}{\nu_i - iq_i} \right)$$

where

f_r is the BRDF

P is the incident power

Ω is the solid angle

dP is the power scattered into solid angle $d\Omega$

$\omega = 2\pi f$; angular frequency

θ_i is the polar angle of incidence

θ_s is the polar angle of scattering

ϕ_i is the azimuthal (off-plane) angle of incidence

ϕ_s is the azimuthal (off-plane) angle of scattering

ε is a dielectric constant

$k_i = (2\pi/\lambda)\sin\theta_i$

$q_i = (2\pi/\lambda)\cos\theta_i$

$k_s = (2\pi/\lambda)\sin\theta_s$

$q_s = (2\pi/\lambda)\cos\theta_s$

$$\nu_i = (k_i^2 - \varepsilon(\omega/c)^2)^{1/2}$$

$$\nu_s = (k_s^2 - \varepsilon(\omega/c)^2)^{1/2}.$$

The quantities in parentheses represent the optical factor. As we mentioned before, this factor is a function of the angles of incidence and scattering and the permittivity (dielectric constant). The optical factors for all directions of polarization, pp, ps, sp, and ss, are shown in Table 2.1. In this table, the first letter stands for the state of polarization of the source, and the second for that of the detector. The letter p stands for polarization parallel to the plane of incidence and s for perpendicular. When the permittivity becomes very large, as for metals in the region we investigated, the quantities in Table 2.1 reduce to those in Table 2.2. When in-plane scattering is evaluated, ϕ_s is zero and the expressions reduce to those in Table 2.3. In our experimental arrangement, we could not measure either pp or ps polarization for all wavelengths because we did not have control over all the polarization orientations. In addition, both sp and ps scattering were undetectable. This is as it should be since $\sin^2\phi$ is identical to zero in both cases. It also implies that ss is equal to su, and pp is equal to pu. These relationships have also been verified by our measurements.

The two-dimensional surface factor or power spectrum is usually assumed to be given by the Lorentzian function, i.e., $2\pi\sigma^2\ell^2/(1+p^2\ell^2)^{3/2}$, where σ is the rms surface height, ℓ is the surface height autocorrelation function length, and p is the surface

Table 2.1. General F_o Expressions.

pp	$\cos^2\phi \times \dfrac{[(\sin^2\theta_i-\varepsilon)^{\frac{1}{2}}(\sin^2\theta_s-\varepsilon)^{\frac{1}{2}}\cos\phi + \varepsilon \sin\theta_i\sin\theta_s]^2}{[(\sin^2\theta_i - \varepsilon \cos^2\theta_i)(\sin^2\theta_s - \varepsilon \cos^2\theta_s)]}$
ps	$\sin^2\phi \times \dfrac{\sin^2\theta_i - \varepsilon}{\sin^2\theta_i - \varepsilon \cos^2\theta_i}$
sp	$\sin^2\phi \times \dfrac{\sin^2\theta_s - \varepsilon}{\sin^2\theta_s - \varepsilon \cos^2\theta_s}$
ss	$\cos^2\phi$

Table 2.2. F_o Expressions for Metals.

pp	$\cos^2\phi \times \dfrac{\lvert\cos\phi - \sin\theta_i\sin\theta_s\rvert^2}{\lvert\cos\theta_i\cos\theta_s\rvert^2}$
ps	$\sin^2\phi/\cos^2\theta_i$
sp	$\sin^2\phi/\cos^2\theta_s$
ss	$\cos^2\phi$

Table 2.3. In-Plane F_o Expressions for Metals.

pp	$\left\| \frac{1 - \sin\theta_i \sin\theta_s}{\cos\theta_i \cos\theta_s} \right\|^2$
ps	0
sp	0
ss	1

spatial frequency, $(2\pi/\lambda)(\cos\theta_s - \cos\theta_i)$. Thus the two governing BRDF equations with which we compared our data are

$$f_r^{ss} = \frac{1}{\pi^2} k^4 \cos\theta_i \cos\theta_s \frac{2\pi\sigma^2\ell^2}{(1+p^2\ell^2)^{3/2}} \tag{2.2}$$

$$f_r^{pp} = \frac{1}{\pi^2} k^4 \cos\theta_i \cos\theta_s \left[\frac{1-\sin\theta_i \sin\theta_s}{\cos\theta_i \cos\theta_i}\right]^2 \frac{2\pi\sigma^2\ell^2}{(1+p^2\ell^2)^{3/2}} . \tag{2.3}$$

Notice that for a given wavelength and angle of incidence the only parameters that can be fit are the rms surface height σ and the correlation length.

The corresponding one-dimensional vector models are shown below, and the transition from the two-dimensional model to the one-dimensional one is given in Appendix A

$$f_r^{ss} = \frac{2}{\pi} k^3 \cos\theta_i \cos\theta_s \frac{2\sigma^2 \ell}{(1+p^2\ell^2)} \tag{2.4}$$

$$f_r^{pp} = \frac{2}{\pi} k^3 \cos\theta_i \cos\theta_s \left[\frac{1-\sin\theta_i \sin\theta_s}{\cos\theta_i \cos\theta_s}\right]^2 \frac{2\sigma^2 \ell}{(1+p^2\ell^2)} . \tag{2.5}$$

Equation (2.4) has two interesting features. For small $\beta-\beta_o$, i.e., small angle of scattering from the surface normal, the equation reduces to

$$f_r^{ss} = \frac{2}{\pi} k^3 \cos\theta_i \cos\theta_s \, 2\sigma^2 \ell ,$$

whereas for large $\beta-\beta_o$ values it becomes

$$f_r^{ss} = \frac{2}{\pi} k^3 \cos\theta_i \cos\theta_s \frac{2\sigma^2}{p^2 \ell} .$$

The intersection of these two asymptotic lines, as shown in Fig. 2.2, is

$$\frac{2}{\pi} k^2 \cos\theta_i \cos\theta_s \, 2\sigma^2 \ell = \frac{2}{\pi} k^3 \cos\theta_i \cos\theta_i \frac{2\sigma^2 \ell}{p^2 \ell^2} . \tag{2.6}$$

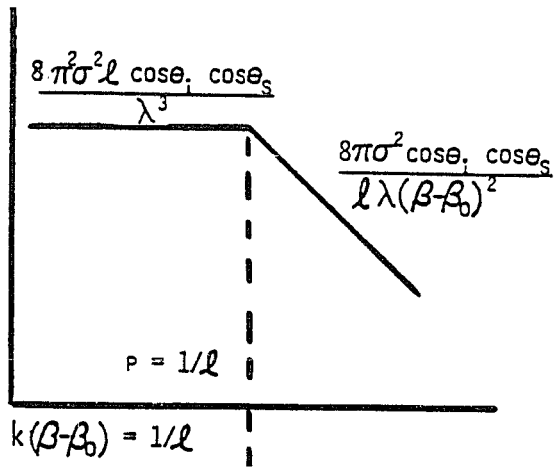

Fig. 2.2. Intersection of Two Asymptotes from One-Dimensional Vector Model (ss).

It can be simplified to

$$p\ell = 1 \tag{2.7}$$

or

$$\frac{2\pi}{\lambda}(\beta-\beta_o) = 1/\ell\ . \tag{2.8}$$

That is, by locating the intersection in the $\beta-\beta_o$ coordinate of the BRDF plot for a specific wavelength, we can obtain the autocorrelation length of the sample under test.

A list of the optical factors used by all authors for the case of $\lambda >> \sigma$ is given in Appendix B. For the case of a metal (real part of ε is negative and much larger in Appendix B than the negative part), we have proved that all optical factors can be reduced to the same form.

Scalar Theories

Scalar theory, which is based on the scalar diffraction integral, Kirchhoff approximation, Fourier transformation, and statistical techniques, has been used by Davies (1954) and Beckmann and Spizzichino (1963) to solve radio and radar waves reflected from sea surfaces and terrain and by Chandley and Welford (1975) to study the light scattered from optical surfaces.

Several authors assume that the surface height distribution is isotropic since the surface statistics used by these authors are the traditional two-dimensional Gaussian autocorrelation function. However, as we mentioned above, the Gaussian function is not in agreement with most of the measurements.

Generally, classical scalar theory has been used successfully to calculate diffraction from obstacles and apertures. Assumptions are made so that the properties of the materials (like conductivity and dielectric constant) do not enter the calculations. No notice is taken of polarization, but if only a single polarization exists in the incident beam and ellipticity is not introduced, the problem is a scalar one. For the metallic sample used and the angles of incidence introduced, vector theory shows that the ellipticity introduced on reflection is negligible.

With this background, we will generalize and extend the scalar theory into the vector regime. Hence, the scalar theory will be used to compare the polarized scattering data so as to verify or deny the above assumptions. All orientations of polarized light will be

treated equally, and we will adopt a reasonable surface power spectrum instead of maintaining the old assumptions of a Gaussian function.

Thus, replacing the optical factors in Eqs. (2.2) through (2.5) with those of Table 2.4, we can obtain the BRDF of scalar theory, which in turn will be compared with the data.

Table 2.4. Surface Factors of Scalar Theories.

Davies (1954):	$(\cos\theta_i + \cos\theta_s)^4/\cos\theta_s$
Beckmann: (Beckmann and Spizzichino, 1963)	$\dfrac{\cos\theta_i(\cos\theta_i + \cos\theta_s)(1 + \cos\theta_i\cos\theta_s - \sin\theta_i\sin\theta_s)}{\cos\theta_s}$
Harvey (1976):	1

Relationship of uu and All Polarizations

It is well known that the optical factor in vector theory is half the sum of pp, ps, sp, and ss (Elson and Bennett, 1979b). To explore the relationship between the uu and all polarization conditions, it is convenient to start from the energy scattered into a solid angle

$$\frac{dP_s^{uu}}{d\Omega} = \frac{1}{2}\left(\frac{dP_s^{ss}}{d\Omega} + \frac{dP_s^{sp}}{d\Omega} + \frac{dP_s^{ps}}{d\Omega} + \frac{dP_s^{pp}}{d\Omega}\right). \qquad (2.9)$$

Here again the superscripts represent the status and directions of polarization; the subscripts stand for the power that is scattered. However, both dP_s^{sp} and dP_s^{ps} are zero since we are making an in-plane measurement only. These two terms can be dropped and Eq. (2.9) reduces to

$$\frac{dP_s^{uu}}{d\Omega} = \frac{1}{2}\left(\frac{dP_s^{ss}}{d\Omega} + \frac{dP_s^{pp}}{d\Omega}\right). \tag{2.10}$$

However, Eq. (2.9) does not quite represent our measurements. The transmittance of the polarizers should be taken into consideration. If the transmittance of the polarizers is τ, Eq. (2.9) becomes

$$\tau \frac{dP_s^{uu}}{d\Omega} = \frac{1}{2}\left(\frac{dP_s^{ss}}{d\Omega} + \frac{dP_s^{pp}}{d\Omega}\right) \tag{2.11}$$

or

$$\frac{dP_s^{uu}}{d\Omega} = \frac{1}{2\tau}\left(\frac{dP_s^{ss}}{d\Omega} + \frac{dP_s^{pp}}{d\Omega}\right). \tag{2.12}$$

Likewise, the relationship of incident energy between unpolarized light and polarized can be expressed as

$$\tau P_i^{uu} = P_i^{ss} = P_i^{pp} \tag{2.13}$$

or

$$P_i^{uu} = \frac{1}{\tau} P_i^{ss} = \frac{1}{\tau} P_i^{pp}. \tag{2.14}$$

Here, the subscript i stands for the power that is incident.

Dividing Eq. (2.13) by Eq. (2.11), we obtain

$$\frac{dP_s^{uu}}{P_i^{uu}d\Omega} = \frac{1}{2}\frac{1}{P_i^{uu}}\left(\frac{dP_s^{ss}}{\tau d\Omega} + \frac{dP_s^{pp}}{\tau d\Omega}\right)$$

$$= \frac{1}{2}\left(\frac{dP_s^{ss}}{(1/\tau)P_i^{ss}\tau d\Omega} + \frac{dP_s^{pp}}{(1/\tau)P_i^{pp}\tau d\Omega}\right)$$

$$= \frac{1}{2}\left(\frac{dP_s^{ss}}{P_i^{ss}d\Omega} + \frac{dP_s^{pp}}{P_i^{pp}d\Omega}\right). \qquad (2.15)$$

The left-hand side is the BRDF of uu; the right-hand side τ's cancel out, and the result is the average BRDF of ss and pp. Equation (2.11) thus can be rewritten as

$$BRDF_{vector}(uu) = \frac{1}{2} BRDF_{vector}(ss+pp). \qquad (2.16)$$

The corresponding relationship is simple and straightforward since scalar theory treats all polarization equally. Therefore, the BRDF of uu is the average of all polarizations, i.e.,

$$BRDF_{scalar}(uu) = \frac{1}{4} BRDF_{scalar}(ss+sp+ps+pp). \qquad (2.17)$$

Since sp and ps have no contribution, Eq. (2.9) becomes

$$\mathrm{BRDF}_{\mathrm{scalar}}(uu) = \frac{1}{2}\,\mathrm{BRDF}_{\mathrm{scalar}}(ss+pp). \tag{2.18}$$

It is interesting that both the scalar and vector theories have the same form although they are derived from different physical foundations. The most important point in this derivation is the difference in the case of off-plane measurements.

Since the contributions from ps and sp are nontrivial, Eq. (2.15) will become

$$\frac{dP_s^{uu}}{P_i^{uu}d\Omega} = \frac{1}{2}\left(\frac{dP_s^{ss}}{P_i^{ss}d\Omega} + \frac{dP_s^{pp}}{P_i^{pp}d\Omega} + \frac{dP_s^{sp}}{P_i^{sp}d\Omega} + \frac{dP_s^{ps}}{P_i^{ps}d\Omega}\right). \tag{2.19}$$

The corresponding BRDF relationship is

$$\mathrm{BRDF}_{\mathrm{vector}}(uu) = \frac{1}{2}\,\mathrm{BRDF}_{\mathrm{vector}}(ss+pp+sp+ps). \tag{2.20}$$

Equation (2.17) for scalar theory still holds since ps and sp cannot be neglected. Comparing Eq. (2.20) and (2.17), we realize that the vector uu BRDF is half the sum of the BRDF for all polarizations, whereas the scalar uu is the average (1/4) of all polarizations.

CHAPTER 3

APPARATUS

This chapter briefly describes the apparatus used to measure BRDF. The instrument was originally built and had been operating in the Infrared Lab, Optical Sciences Center, for several years. The current version was designed by Larry Brooks. A general description is given here. For further details, see Brooks (1982).

The instrument is a multiple-wavelength, microcomputer-controlled, two-phase system, i.e., it can be operated either manually or automatically. It has the capacity of operating at any of the following wavelengths: 0.6328 μm, 1.15 μm, 3.39 μm, and 10.6 μm. A Z80 microprocessor monitors and controls the mechanical modules, lock-in detection, data calculation, and storage on a floppy disk. It also interfaces with a Tektronix 4051 desk-top computer for data analysis and graphic display. Figure 3.1 is a photograph of the instrument.

Figure 3.2 is a block diagram of the complete system, and Fig. 3.3 is the optical layout. A selected laser beam passes through a collimator, spatial filter, reflective chopper, array of attenuators, and image-forming optics and irradiates the sample under test.

To admit the desired wavelength, a kinematically relocatable mirror must be positioned appropriately. The mirror is shown in all three of its positions in Fig. 3.3 to demonstrate how the beams are admitted. If the mirror is at position "a" then the 0.6328-μm He-Ne

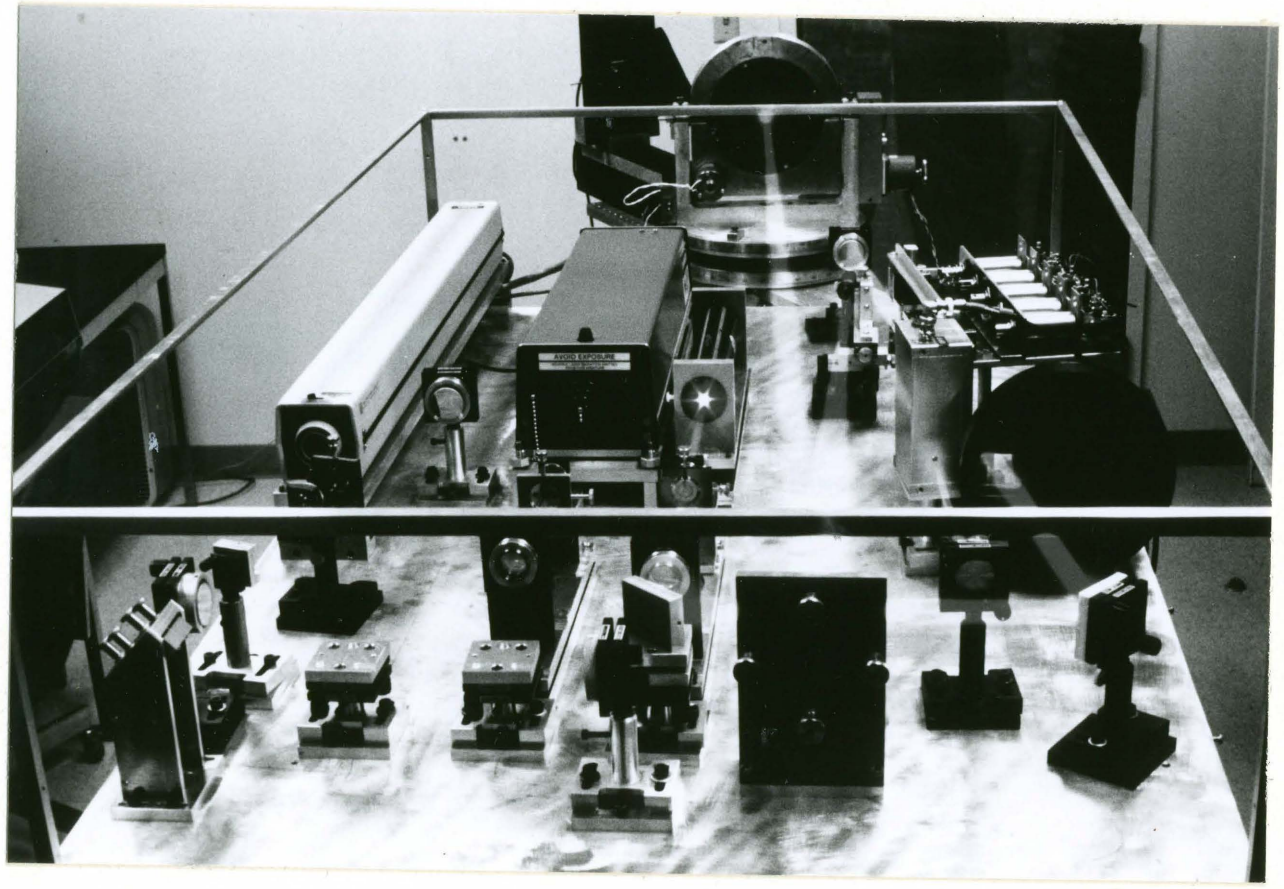

Fig. 3.1. Photograph of BRDF Measurement Facility.

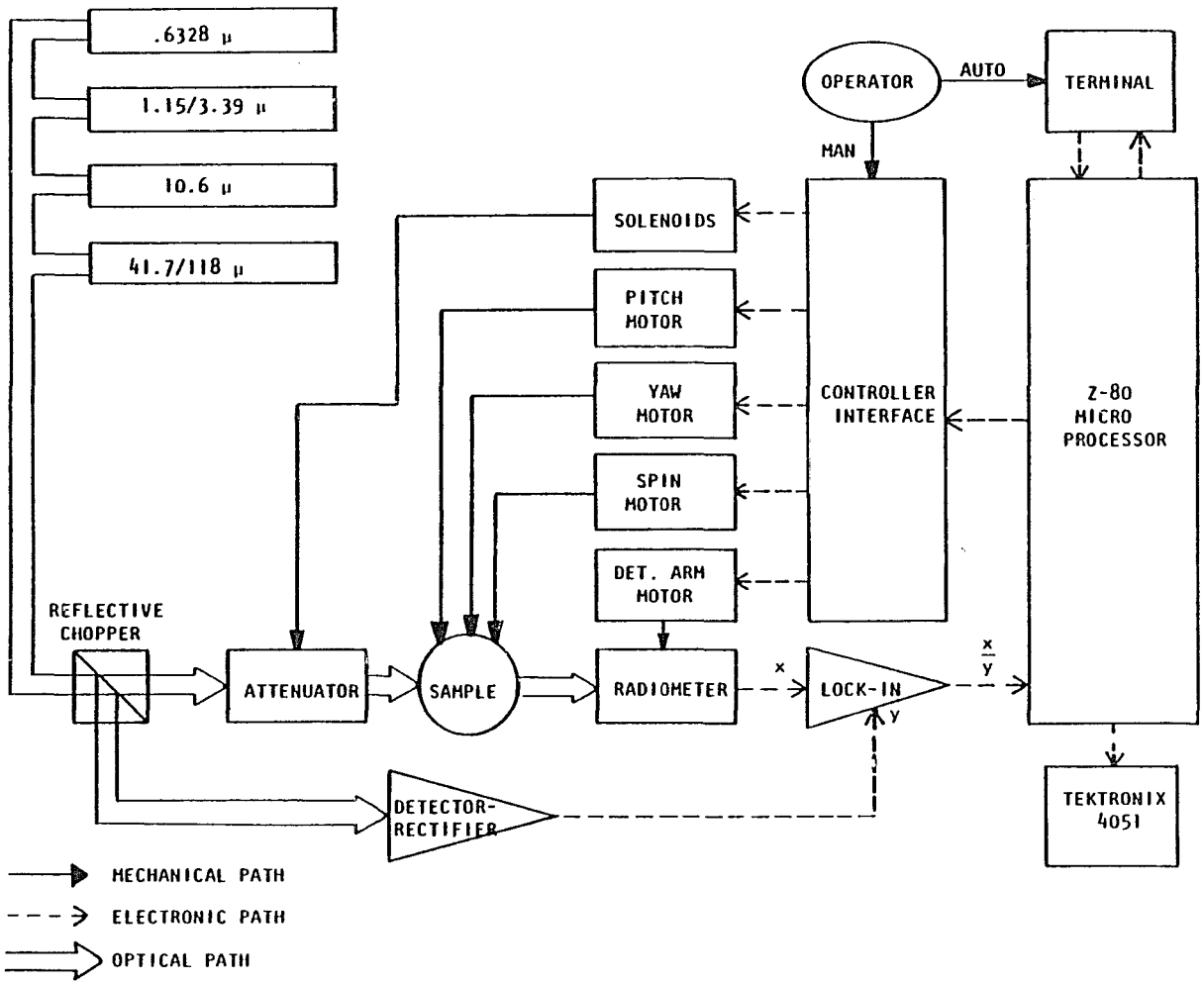

Fig. 3.2. System Block Diagram. (From Brooks, 1982.)

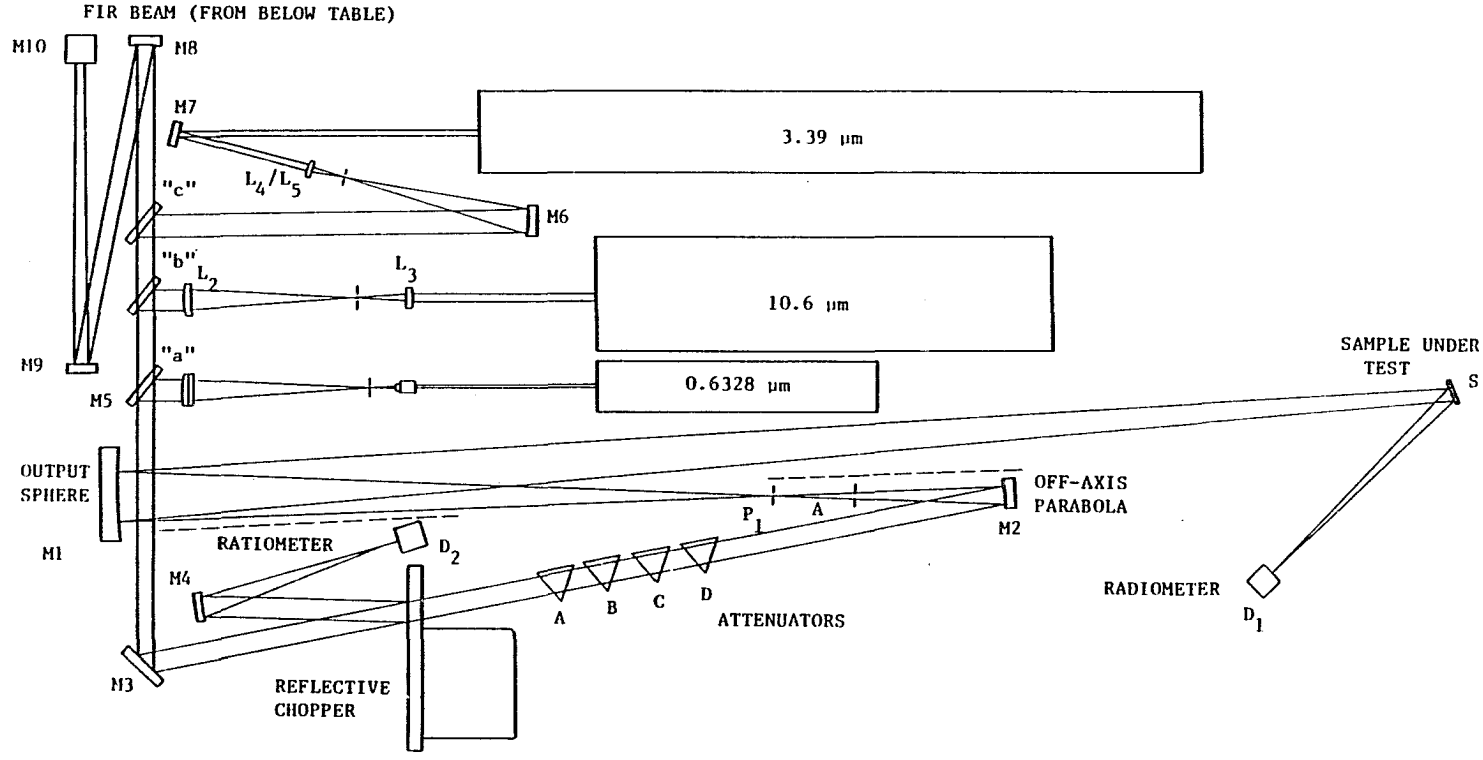

Fig. 3.3. Optical Layout, Upper Level.

Dashed lines represent baffles. M5 is kinematically repositionable to positions "a," "b," and "c." (From Brooks, 1982.)

beam irradiates the sample; at position "b" the 10.6-μm CO_2 beam does; and at position "c" the 3.39-μm beam does. The F/40 output spherical mirror located at position M1 (see Fig. 3.3) focuses the beam on the sample, with a beam diameter of 1 cm at every wavelength.

The sample can be pitched or yawed in a controlled manner to provide the scattering characteristic for a specific orientation. The scattered radiation is sampled at selected angles by a detector that moves about the sample in the incident (horizontal) plane on a boom. For different wavelengths, different types of detectors are used. Table 3.1 shows the specifications and some of the features of each detector.

The chopped radiation collected by the detector is amplified and transmitted to a lock-in amplifier. The digitized signal out of the lock-in amplifier is then output to a microprocessor. During measurement, the scattered radiation is sampled 50 to 100 times and averaged. An algorithm in the microprocessor calculates the averaged data and yields the corresponding BRDF value in real time. Data collected by the microprocessor are stored on a floppy disk for future use. The information stored on the disk may be transferred to a Tektronix computer for data analysis, plotting, and further study.

A laminar flow bench directs a stream of filtered air across the sample to keep it clean during measurements.

The scheme we applied to measure the BRDF is the so-called "definition method" or "straight-through method." The equation for BRDF is

Table 3.1. Detectors Used in the Study.

Wavelength:	0.6328 μm	1.15 μm	3.39 μm	10.6 μm	10.6 μm
Detector:	(1) GaAsP (2) Si	Ge	(1) PbS (2) PbSe	Si:As	HgCdTe
T:	277 K	277 K	196 K	4 K	77 K
Amplifier:	Amplifier box on bench	Amplifier box on bench	Amplifier box on bench	Amplifier box on bench	Amplifier box on optics rail
Power supply:	11 V ac box on bench	11 V ac box on bench	Batteries in amplifier box	Batteries in amplifier box	Batteries in amplifier box
Bias:	N/A	N/A	Internal battery	Internal battery	N/A
Lens:	Glass, F/1 or telescopic	Glass, F/1 or telescopic	BaF_2, F/1	BaF_2, F/1	ZnS 2.3-mm-diameter telescopic
Filter:	None	None	3.39-μm narrow-band over detector, cooled	None	

Data courtesy of Lang Brod, Optical Sciences Center

$$\text{BRDF} = \frac{V_S}{V_O \Omega_O \cos P_S \cos(D_S - Y_S)} \tag{3.1}$$

where

V_S = measured signal

V_O = total signal (on-axis, no sample)

Ω_O = solid angle of detector aperture

D_S = detector angle position for sample

Y_S = yaw angle of sample

P_S = pitch angle of sample.

The essence of this technique is based on the balance or symmetric no-sample beam profile (instrumental scattering profile), which is caused mainly by scattering from the focusing mirror and from internal reflection and diffraction.

We were able to achieve a symmetrically distributed no-sample profile by trial-and-error adjustment of the tilt, yaw, and pitch of the detector. Thus we are confident that the measured BRDF is not limited by background noise or instrumental noise. An improper alignment, however, could cause the no-sample profile in one arm to be several times higher than that in the other arm, and the resulting data would be difficult to interpret. This occurs to some extent because the BRDF is additive; that is, noise can be added to the BRDF of the sample.

After the instrument is aligned and the no-sample beam profile appears to be symmetric, the detector is rotated back to the center to ensure that the signal remains at peak value. The voltage reading of the lock-in amplifier is V_o and the BRDF is equal to $1/\Omega_o$, since $V_s = V_o$ and $\cos P_s \cdot \cos(D_s - Y_s) = 1$ in Eq. (3.1). Having stored V_o in the microprocessor, the sample is set up on the sample holder with the desired pitch and yaw angles, and the detector is moved to the desired angle where it measures V_s. This voltage, corrected for the lock-in scale and optical attenuation, is used in Eq. (3.1) to find the BRDF for this specific orientation.

The advantage of this method compared to the "reference sample method" (Bartell, Dereniak, and Wolfe, 1980) is that there is no need to find an ideal reference sample to compare with. However, the use of Eq. (3.1) makes it difficult to determine the solid angle Ω_o of the detector, causes possible overfill of the detector, and complicates the calibration of the attenuator array. The last two problems have been discussed by Brooks (1982); the first problem we will discuss here.

The distance between a sample and a detector can be determined to reasonable accuracy fairly easily. The size of the aperture located in front of the collecting lens of a detector should be as similar as possible to that of the laser beam. If the laser beam size is larger than the aperture, then light will be scattered and diffracted by the edge of the aperture. Thus stray radiation could be added to the detector sensor area, and the lens factor might be

inaccurately calibrated for larger scattering angles. On the other hand, too large an aperture will yield a misleading solid angle Ω_o value. To attack this problem, several different sizes of apertures were used to fit the laser beam size. The voltage readings in the lock-in amplifier were checked with different apertures in place and without an aperture. By trial and error, we were able to find a good aperture and thus an accurate solid angle Ω_o.

CHAPTER 4

DATA PRESENTATION AND COMPARISONS

In this chapter two approaches are used to compare measurements: the bidirectional reflectance distribution function (BRDF) and the associated power spectrum of the surface height distribution. The data presented and the techniques used to reduce the data are discussed in detail, and comparisons are given after each presentation.

BRDF Measurements

BRDF measurements are useful only if the data are not limited by instrumental noise or background noise. Instrumental noise, which is caused mainly by the focusing mirror, was discussed in Chapter 3. Background noise is created by ambient light and thermal radiation.

Figure 4.1 shows the instrument profiles and noise levels for the indicated wavelengths and incidence angles for a 3-in.-diameter fused silica flat coated with aluminum. Several items should be noted in these figures. First, the plots are logarithmic in both scales. Second, the abscissa is in terms of $\beta-\beta_0$, which is $\sin\theta_s-\sin\theta_0$ where θ_0 is the angle of specular reflection. There is a symmetry to these measurements. One can measure, for instance, 10° on either side of the specular direction. The symmetry is limited, however, in that when the sample is tilted, the detector can be on the same side as the sample normal or on the opposite side with the input laser. We have

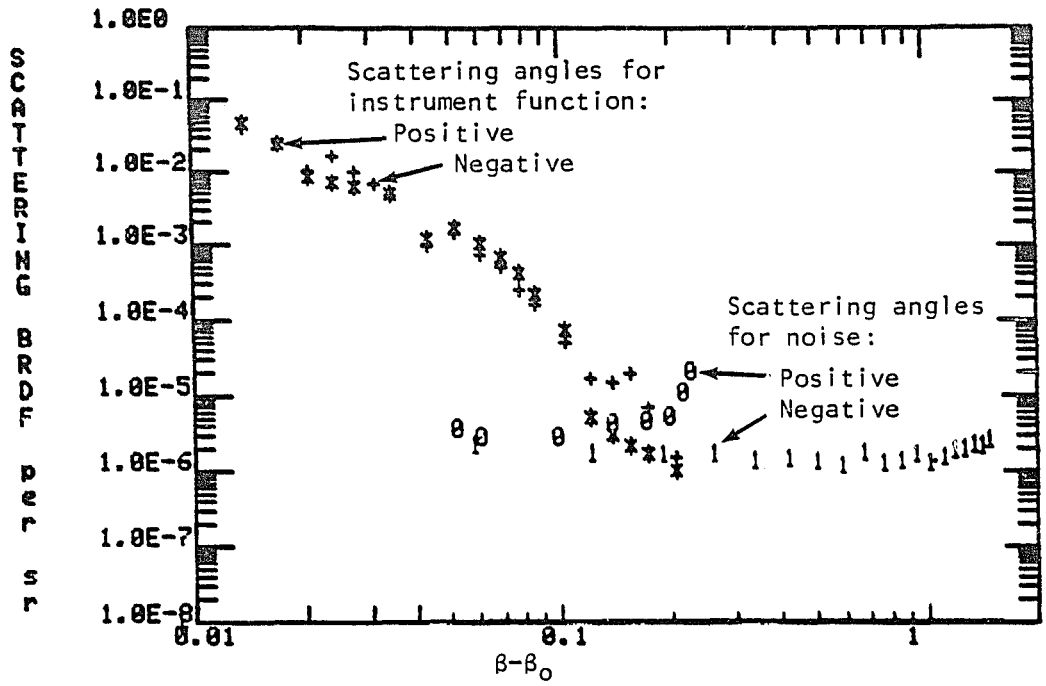

a. 0.6328 μm, 30° incidence

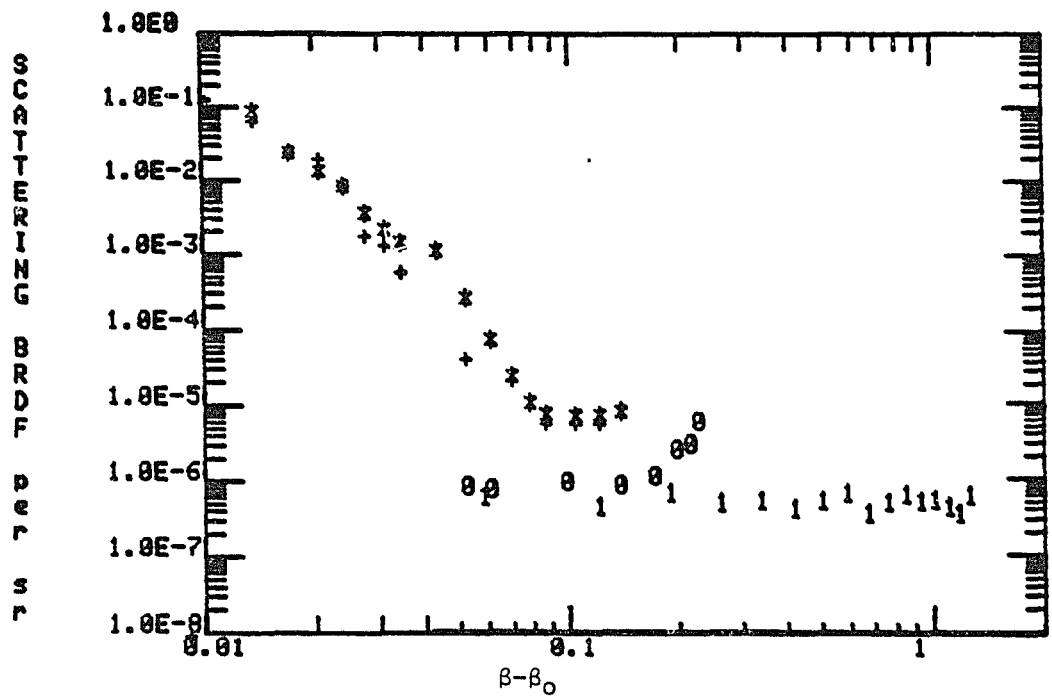

b. 3.39 μm, 30° incidence

Fig. 4.1. Instrument Function and Noise at Three Wavelengths.

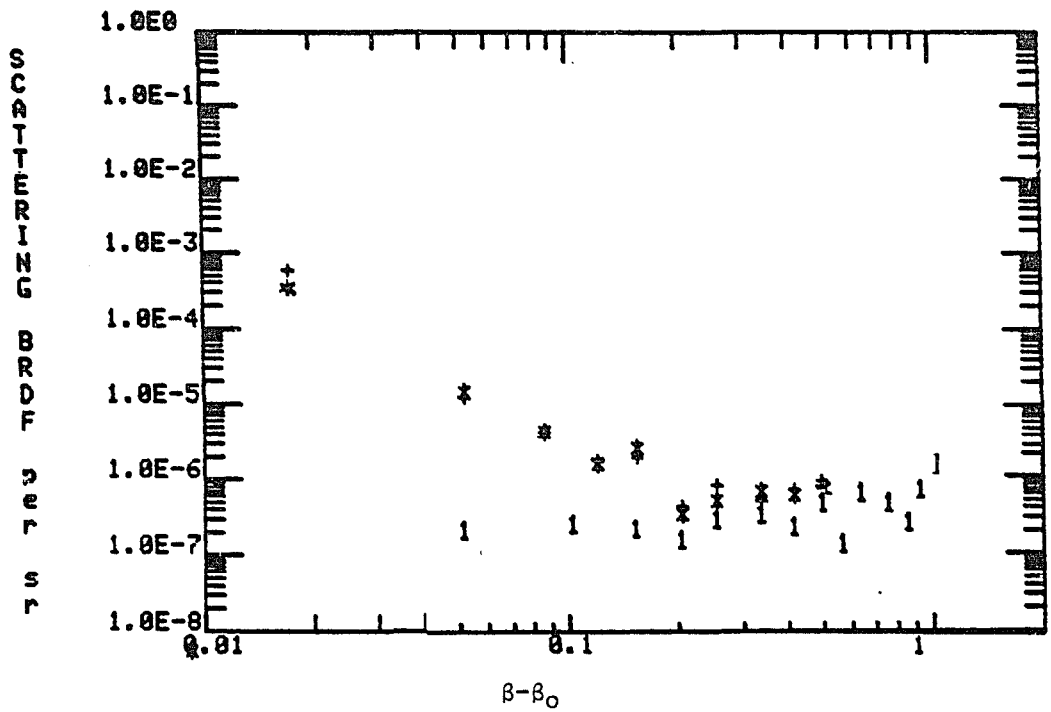

c. 10.6 μm, 30° incidence

Fig. 4.1. Instrument Function and Noise at Three Wavelengths (Continued).

indicated these two situations as positive and negative incidence angles. It is also possible to have positive and negative values for $\beta-\beta_o$. Next, the system profile is generally a curve from about 0.1 on the BRDF scale at $\beta-\beta_p = 0.01$ to about 10^{-5} at $\beta-\beta_o = 0.1$. Data corresponding to $\beta-\beta_o$ values of less than about 0.1 may be contaminated by the system profile. Finally, the noise equivalent BRDF is not constant but can increase without limit as $|\theta_s|$ approaches $|\theta_i|$. These limits are shown schematically (and approximately) in the data curves. Figure 4.2 shows a typical data curve for $\lambda = 0.6328$ μm, $\theta_i = -50°$. The data values are well above the noise values.

Comparisons

Figure 4.3a is the first comparison of theory and experiment. The data are shown as points and the theory as lines. The curves are of the BRDF for ss polarization, the exponential model, 10° angle of incidence and three different wavelengths. It appears that the 0.6328-μm curve may be characteristic of the material (not affected by the instrument profile) almost to $\beta-\beta_o = 0.01$ although the instrument profile does influence the two longer wavelength curves. The theoretical ss curves have all been fit using 26.6 Å for the value of the rms surface height. The correlation distance ℓ was found by trial and error in order to obtain the best fit to the experimental data. Notice, however, that the intersection of the two asymptotes occurs for a value given by $p = 1/\ell$. This intersection can be found for the 10.6-μm curves and has an ℓ value of 10 μm (Fig. 4.3b).

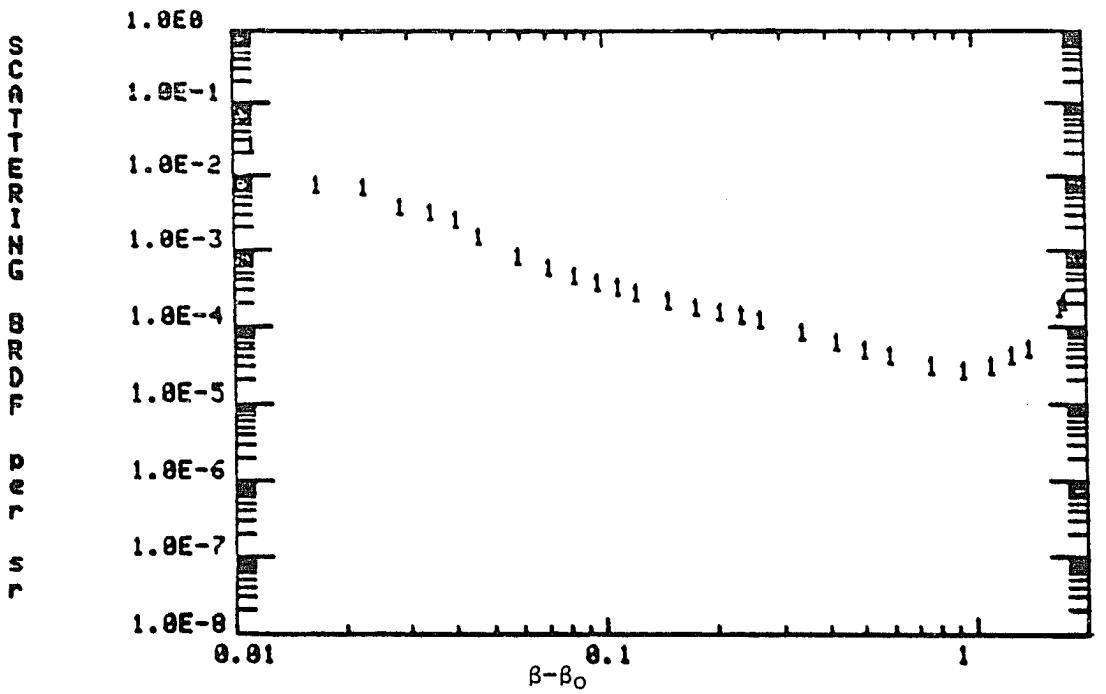

Fig. 4.2. Typical Data Curve.

λ = 0.6328 μm, θ_i = -50°

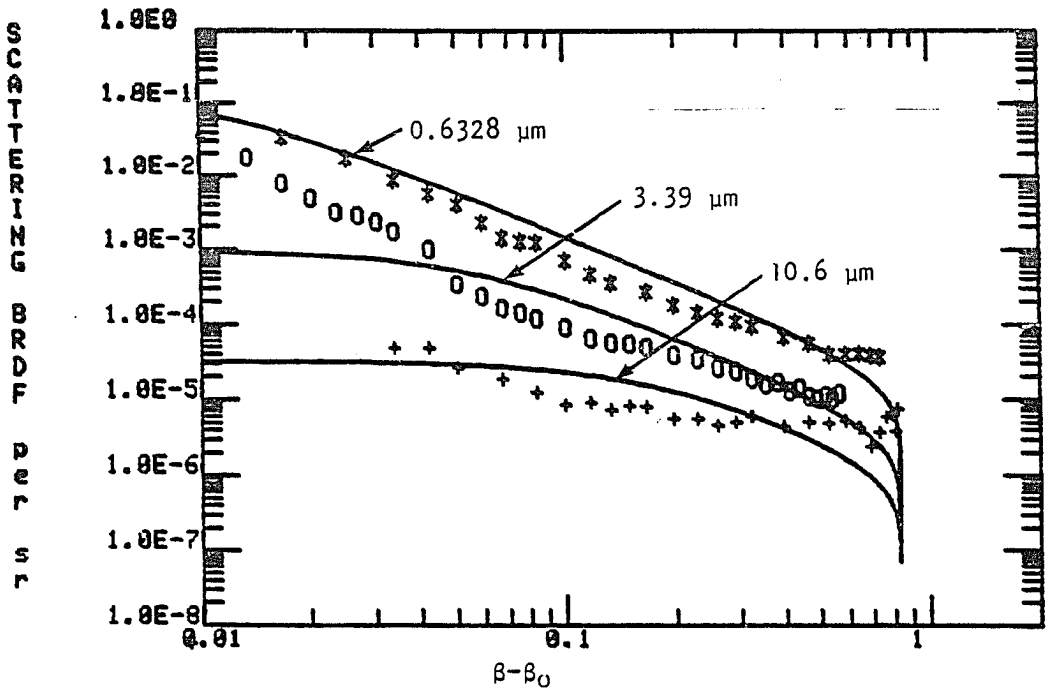

a. 10° incidence

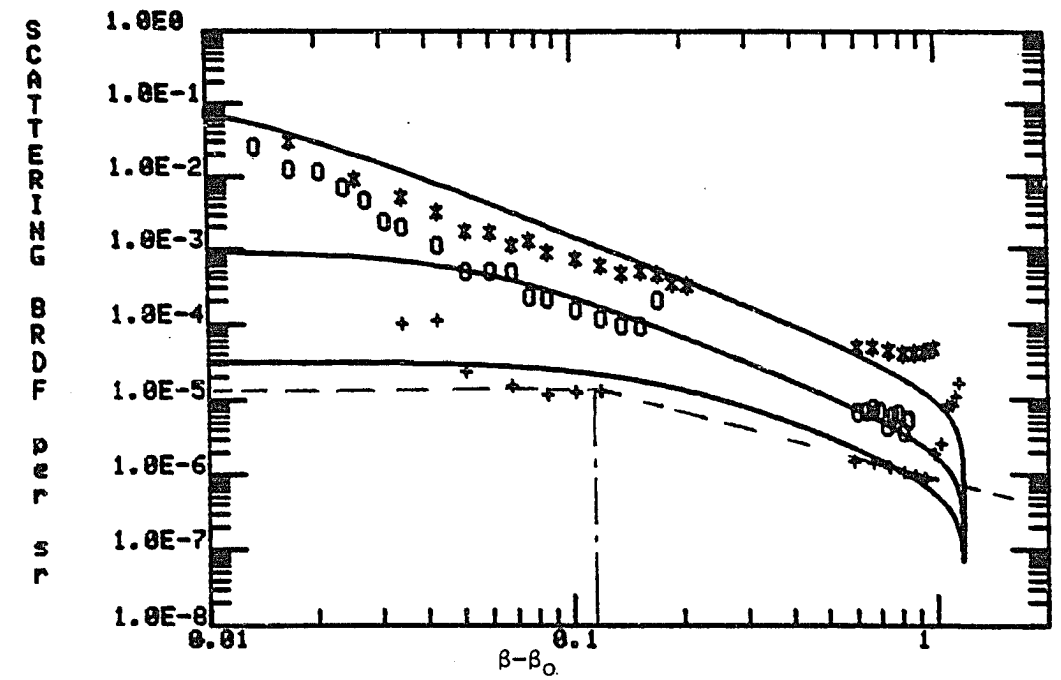

b. -10° incidence

Fig. 4.3. Comparison of Theory and Data, ss Polarization, for 0.6328 μm, 3.39 μm, and 10.6 μm.

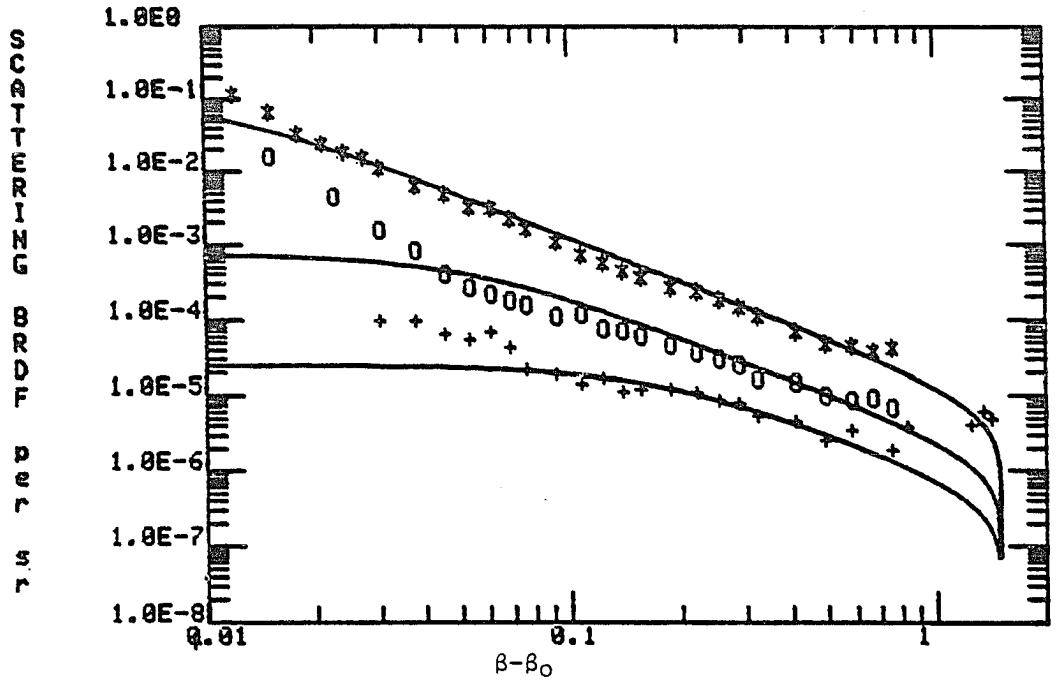

c. -30° incidence

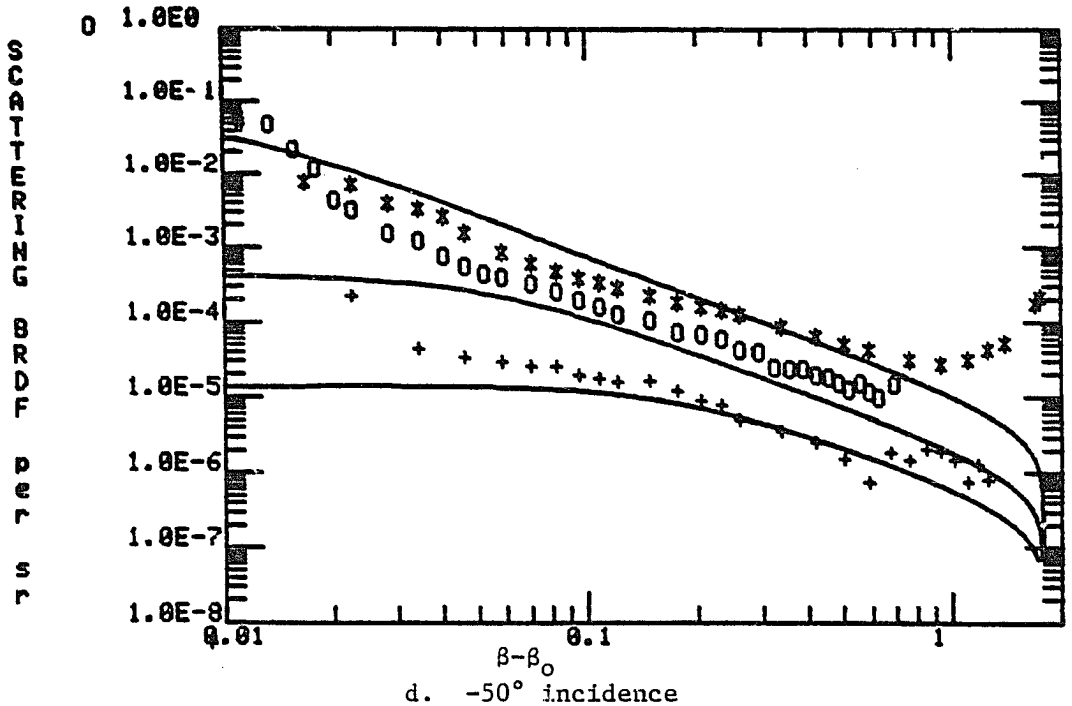

d. -50° incidence

Fig. 4.3. Comparison of Theory and Data, ss Polarization, for 0.5328 μm, 3.39 μm, and 10.6 μm (Continued).

Note that the theoretical curves drop down at large values of $\beta-\beta_o$ whereas the experimental data curl up. We have no firm explanation of this, but we speculate that the discrepancy could be the result of particulates and multiple reflection at large angles. The data are well above the noise values and above most of the noise "curlup." Figure 4.3b shows similar data for a different angle of incidence. In this case the 10.6-μm data are affected by noise at extreme angles. Figures 4.3c and 4.3d show two more examples. The same values of σ and ℓ are used for all curves.

The next set of data, for the pp-polarization arrangement, is shown in Fig. 4.4. The p-polarization theoretical curves curl up at large values of $\beta-\beta_o$ in contrast to the ss values. This happens in about the same way as the noise increases and for the same reason. Thus, determining whether there is a real curl in the data is difficult. We have used 0.488 μm, 0.5165 μm, and 0.6328 μm for these comparisons because our 3.39-μm and 10.6-μm lasers could not be polarized in the p orientation. Similarly, unpolarized measurements could be made only at 0.6328 μm, whereas for polarized measurements the data and theory agree better at small angles of incidence. The data for unpolarized radiation agree with the theory better at larger angles, as shown in Fig. 4.5.

Power Spectra

In the previous approach, we compared the BRDF measurements with theoretical predictions. However, such a comparison requires an assumption about the form of W(p) as defined in Eqs. (2.4) and (2.5).

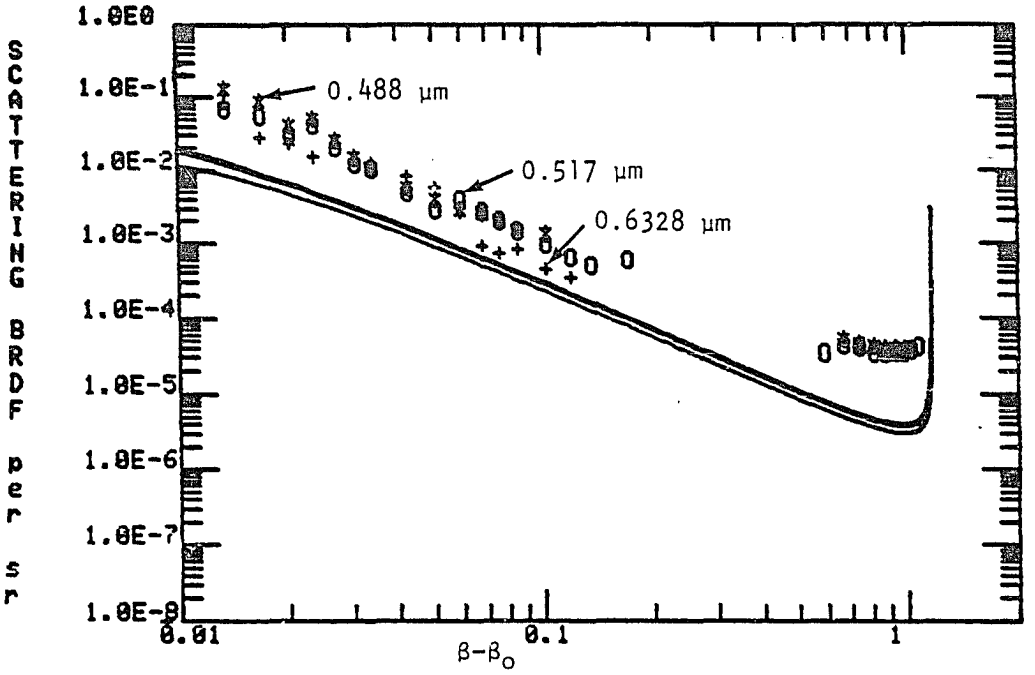

a. -10° incidence

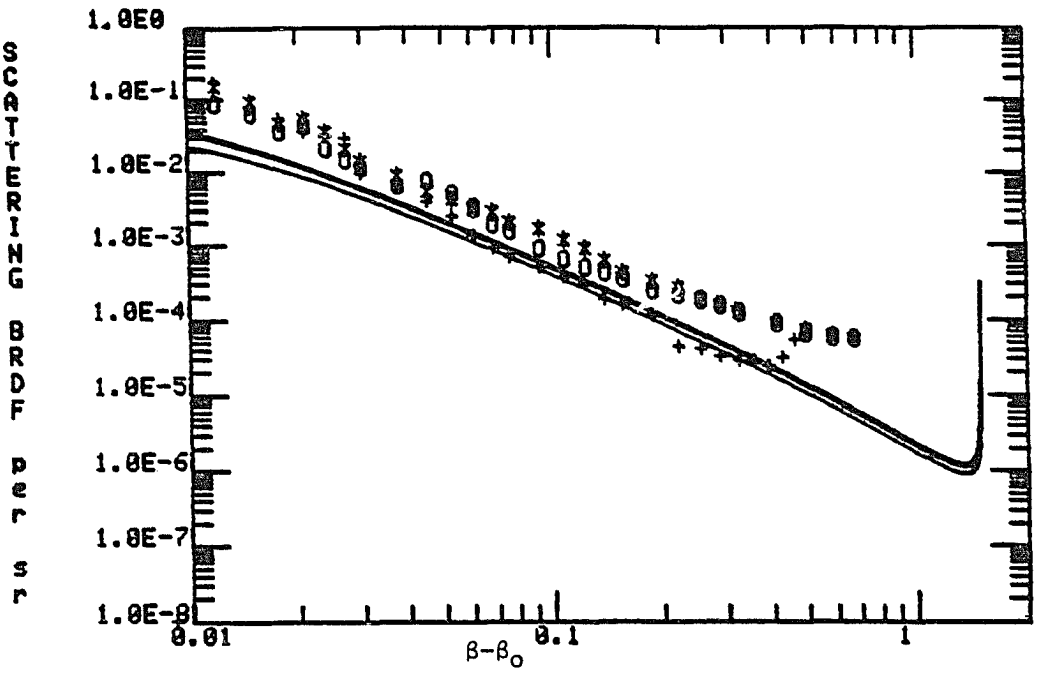

b. -30° incidence

Fig. 4.4. Comparison of Theory and Data, pp Polarization, for 0.488 μm, 0.517 μm, and 0.6328 μm.

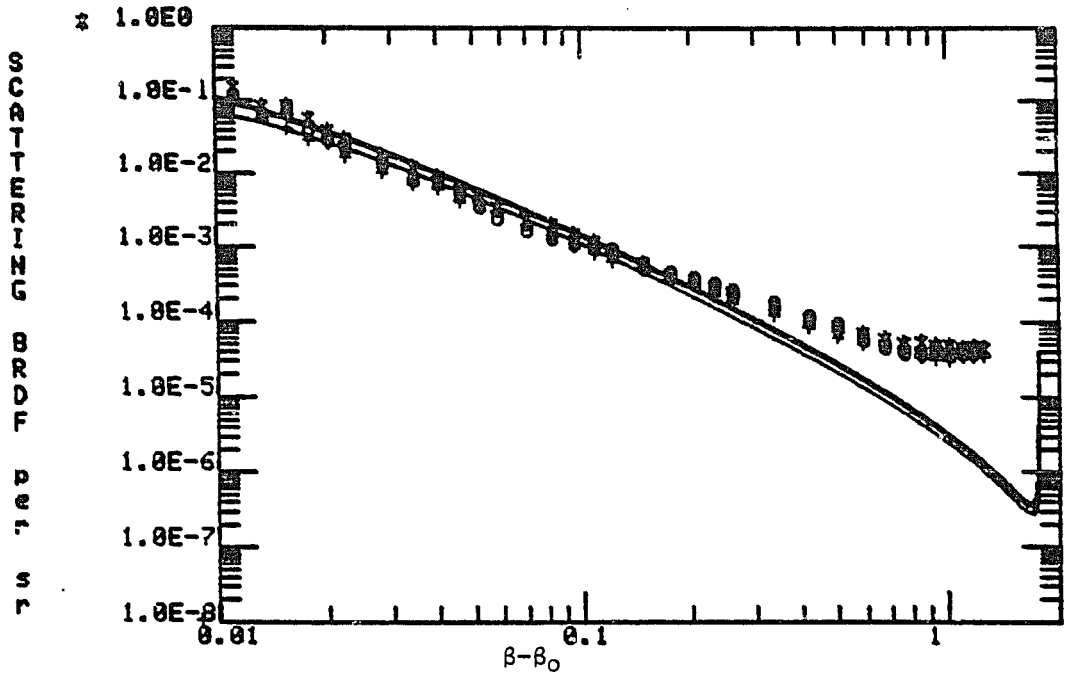

c. -50° incidence

Fig. 4.4. Comparison of Theory and Data, pp Polarization, for 0.488 μm, 0.517 μm, and 0.6328 μm (Continued).

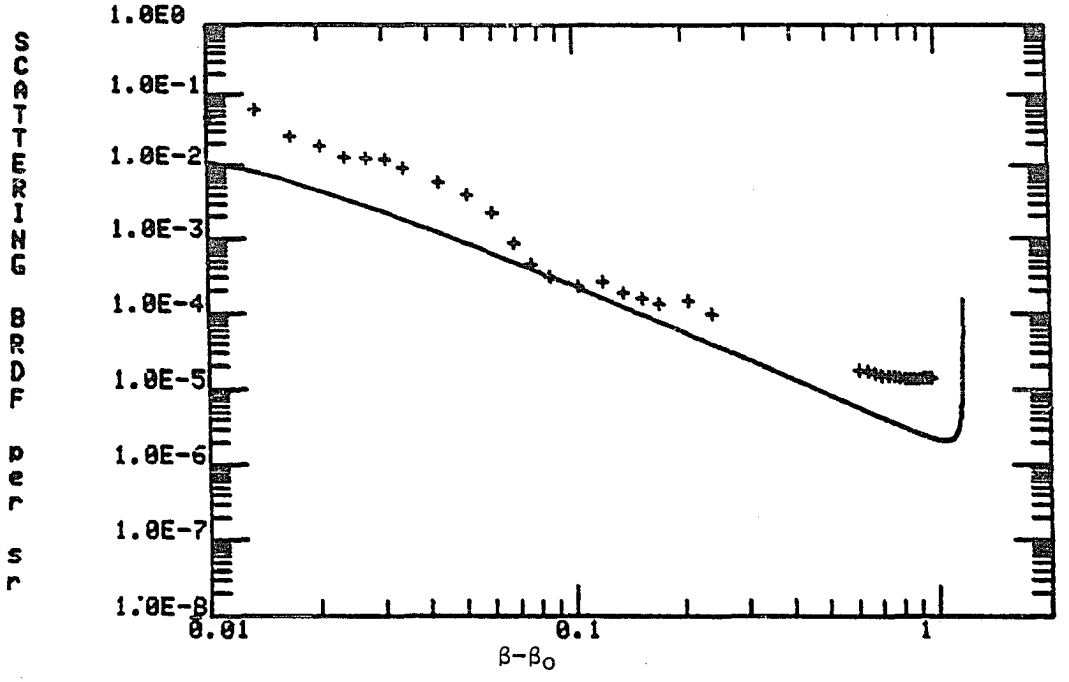

a. 10° incidence

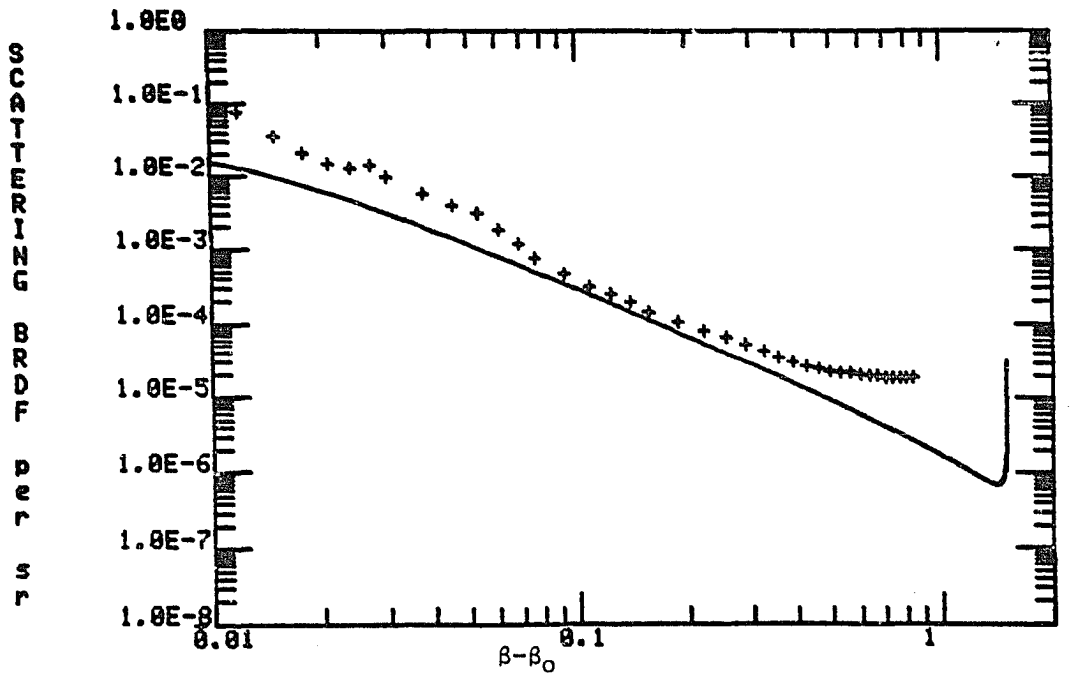

b. 30° incidence

Fig. 4.5. Comparison of Theory and Data, Unpolarized Radiation, for 0.6328 μm.

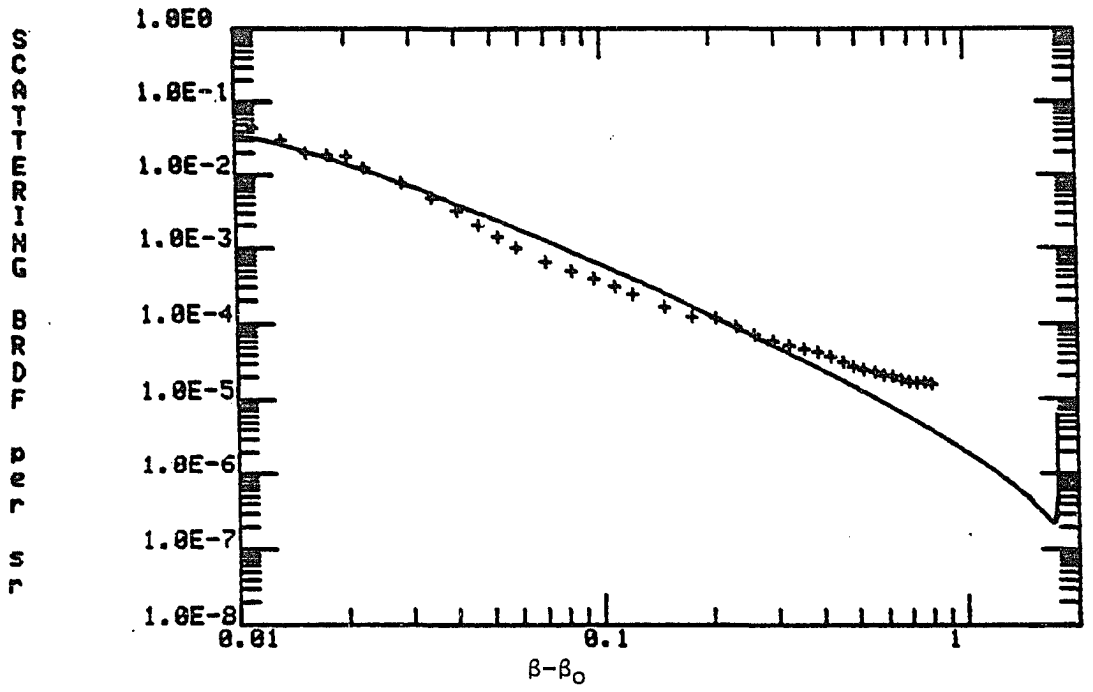

c. 50° incidence

Fig. 4.5. Comparison of Theory and Data, Unpolarized Radiation, for 0.6328 μm (Continued).

Therefore, for the power spectrum measurements, we have made no initial assumptions about the power spectral density of the surface. The two-dimensional power spectrum can be derived from Eqs. (4.1) or (4.2). We divide the measured BRDF data by k^4 and the appropriate optical factor of the corresponding theory and polarization, i.e.,

$$W(p) = \frac{BRDF_{data}}{\frac{1}{\pi^2} k^{4F}} . \tag{4.1}$$

Similarly, from Eq. (4.3) or (4.4), we can obtain the following one-dimensional power spectrum:

$$W(p) = \frac{BRDF_{data}}{(2/\pi)k^{3F}} . \tag{4.2}$$

In this approach, we start from the scalar theory and follow it with vector theory. The power spectrum generated with the two-dimensional Beckmann theory for ss data is shown in Fig. 4.6a. The plot is logarithmic in both scales and the abscissa is in frequency p. The "+" represents the power spectrum of 10.6 μm, "o" the spectrum of 3.39 μm, and "*" the spectrum of 0.6328 μm. Except for a few points at the end of each spectrum, the three spectra are almost parallel. The surface-height power spectrum is a multiple-valued function for most of the spectra. It is as if each wavelength sees a different surface for the same single sample. That certainly cannot be true. However, it is not

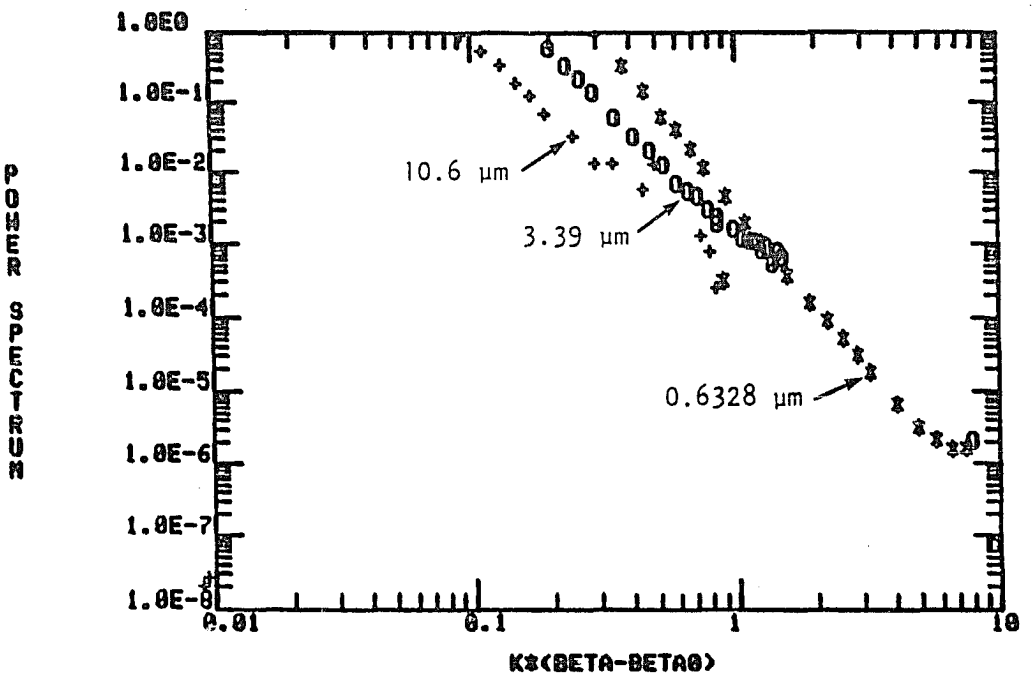

a. Two-dimensional model, 30° incidence

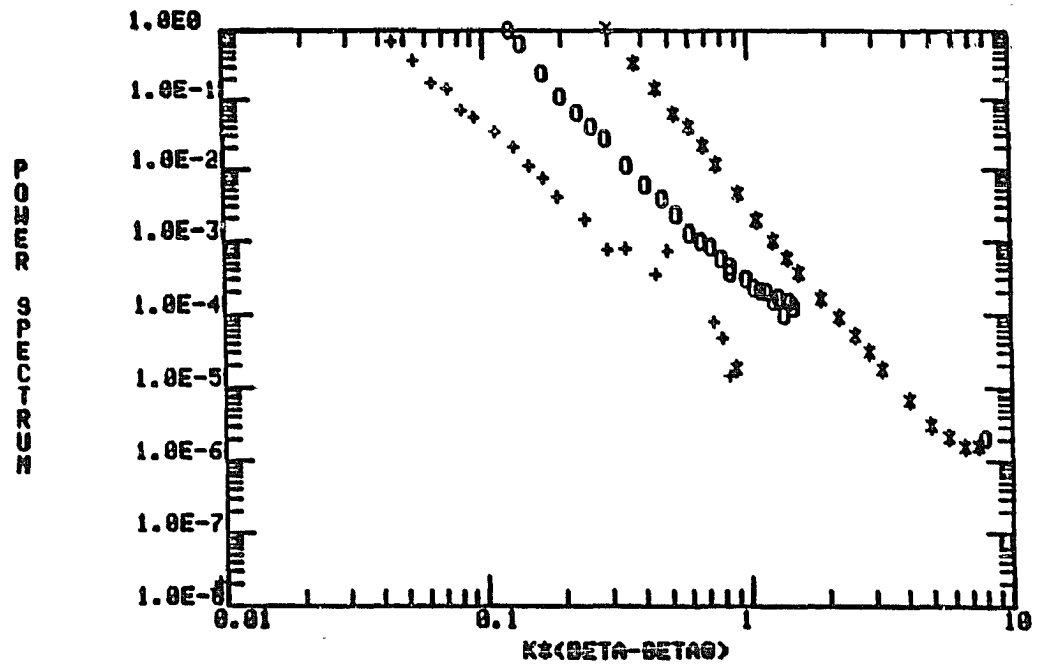

b. One-dimensional model, 30° incidence

Fig. 4.6. Power Spectra for Beckmann Models, for 0.6328 μm, 3.39 μm, and 10.6 μm.

unreasonable to assume the spectrum is one-dimensional rather than two-dimensional. The one-dimensional Beckmann model, Eq. (4.6), is shown in Fig. 4.6b. The fit is terrible, the spectra are not continuous, and the curve is fragmented. Therefore, it is worthwhile to try the other scalar theory. The two- and one-dimensional scalar models are shown in Fig. 4.7. They are not satisfactory at all and are even worse than those of Beckmann. Thus, we must conclude that these scalar formulations of the geometrical factor must be wrong.

The two-dimensional vector power spectrum is shown in Fig. 4.8a. The continuous line is the two-dimensional Lorentzian model with the appropriate values of σ and ℓ. It is clearly a better fit than the previous ones. However, it is still multiple-valued.

Figure 4.8b shows a one-dimensional power spectrum fit for 30° incidence. Again the continuous line is the one-dimensional Lorentzian model. As mentioned before, the plot is power spectrum against surface wave number (frequency) and is defined as $(2\pi/\lambda)\ (\sin\theta_s - \sin\theta_i)$. Thus, the spectrum is a function of wavelength and angles of incidence and scattering. It is also limited by the instrumental profile at low frequencies and by the nonsurface-roughness effect at high frequencies. At first, it seems that it is still double-valued in some regions. For instance, in the region between 1 and 2 μm^{-1}, the lower curve is the 0.6328-μm spectrum, and the upper one is the end of the 3.39-μm spectrum at a larger scattering angle. The end of the curve is not the real contribution of the surface roughness scattering. Similarly, in the region from 0.3 to 0.8 μm^{-1}, the lower set of data is

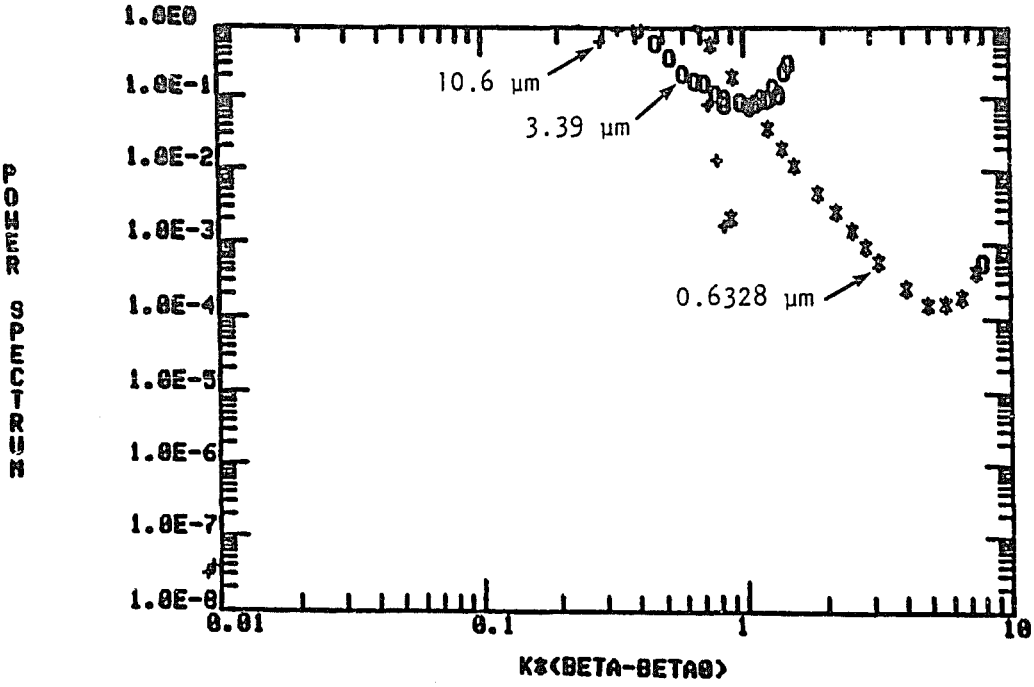

a. Two-dimensional model, 30° incidence

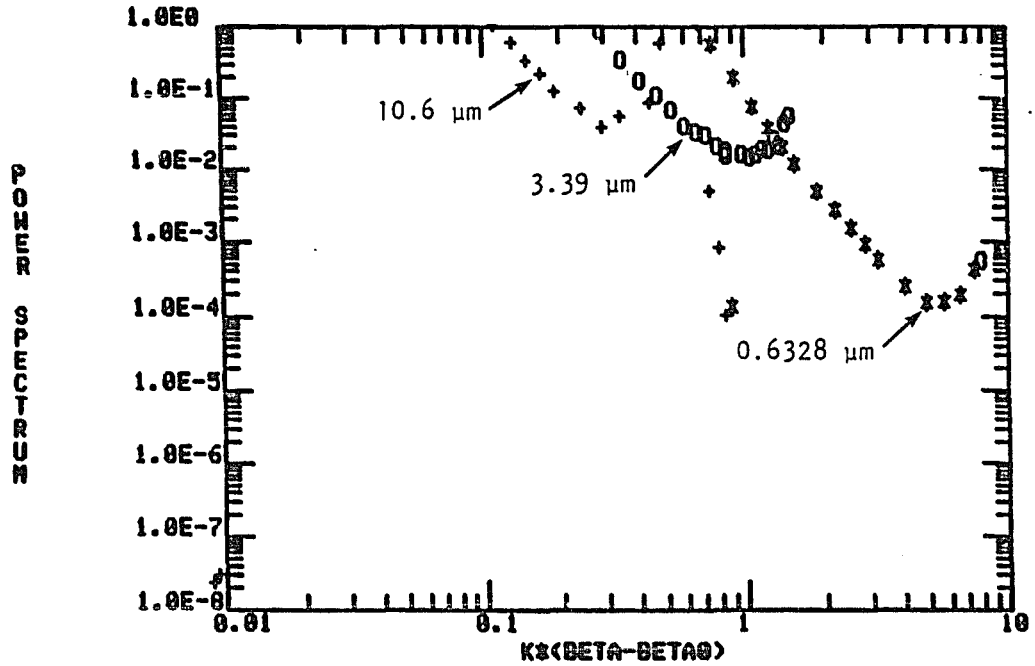

b. One-dimensional model, 30° incidence

Fig. 4.7. Power Spectra for Davies Models, for 0.6328 μm, 3.39 μm, and 10.6 μm.

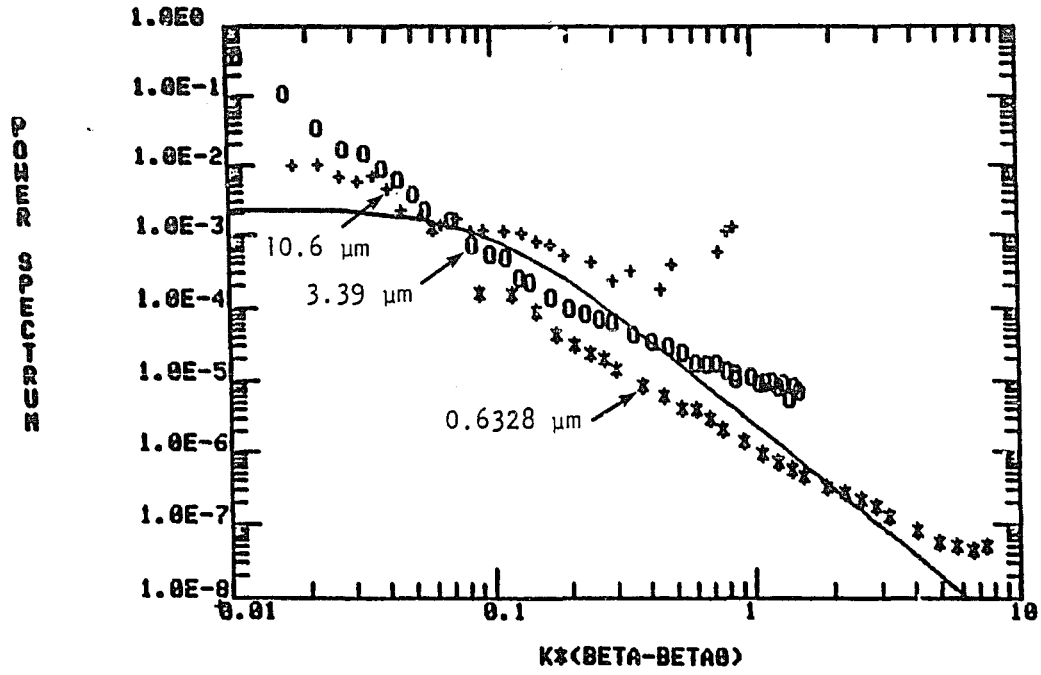

a. Two-dimensional, -30° incidence

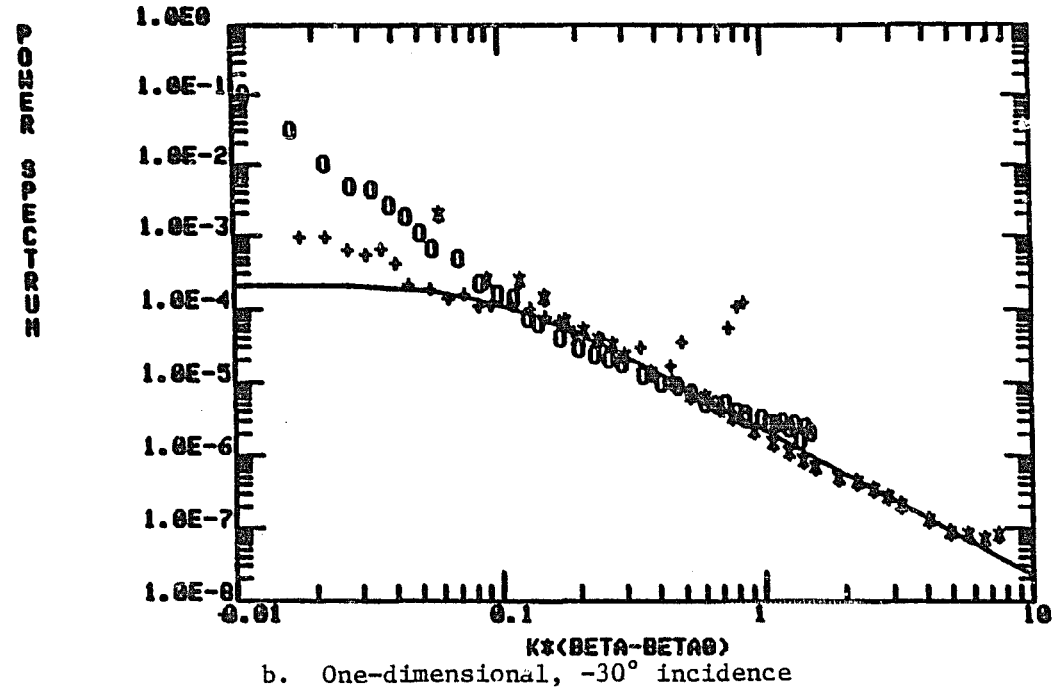

b. One-dimensional, -30° incidence

Fig. 4.8. Power Spectra for Vector Theory and Corresponding Theoretical Curves, for 0.6328 μm, 3.39 μm, and 10.6 μm.

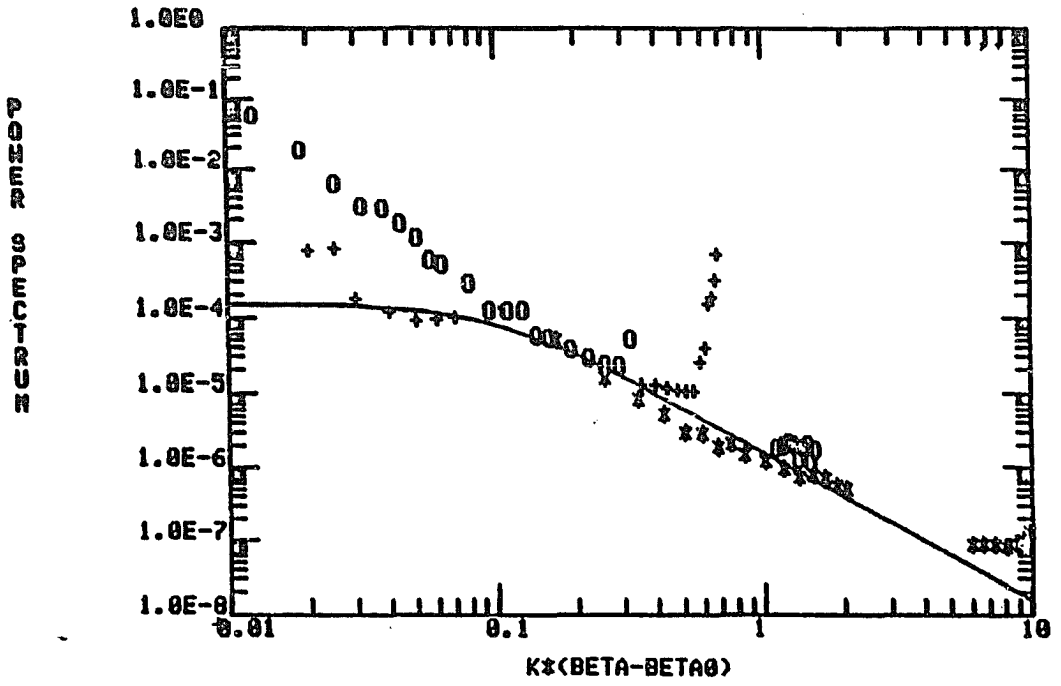

c. One-dimensional, -10° incidence

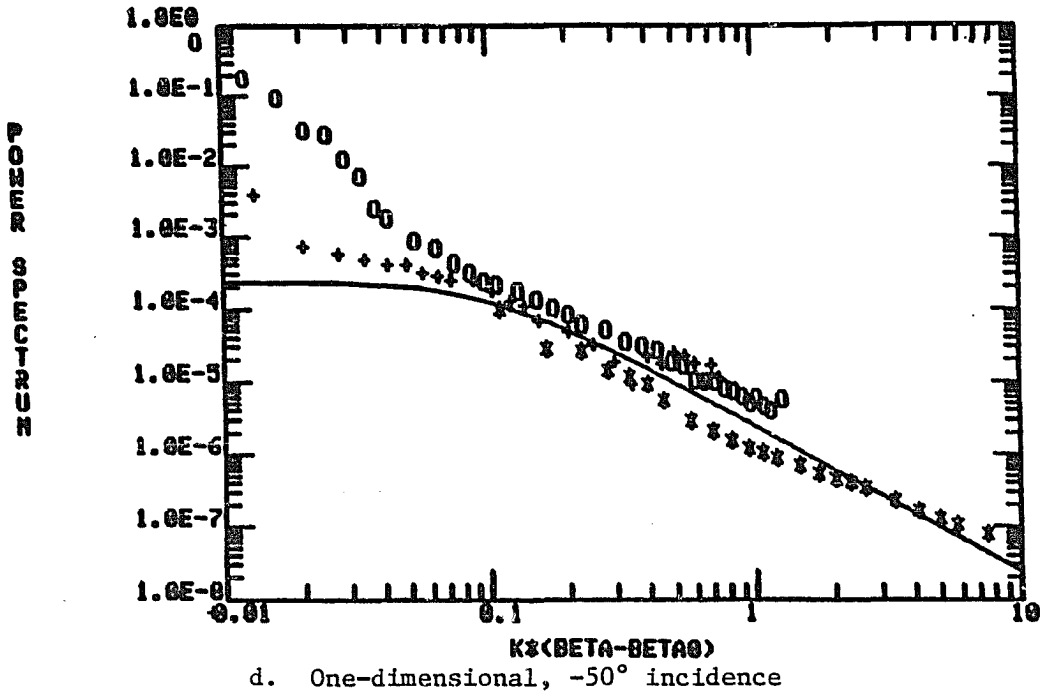

d. One-dimensional, -50° incidence

Fig. 4.8. Power Spectra for Vector Theory and Corresponding Theoretical Curves, for 0.6328 μm, 3.39 μm, and 10.6 μm (Continued).

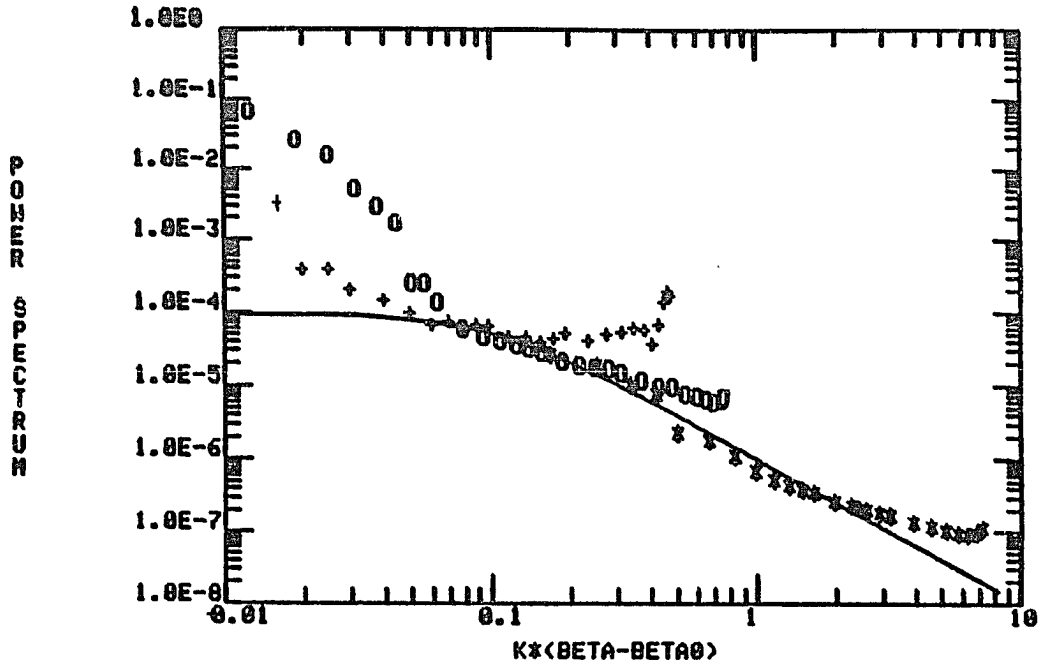

e. One-dimensional, 10° incidence

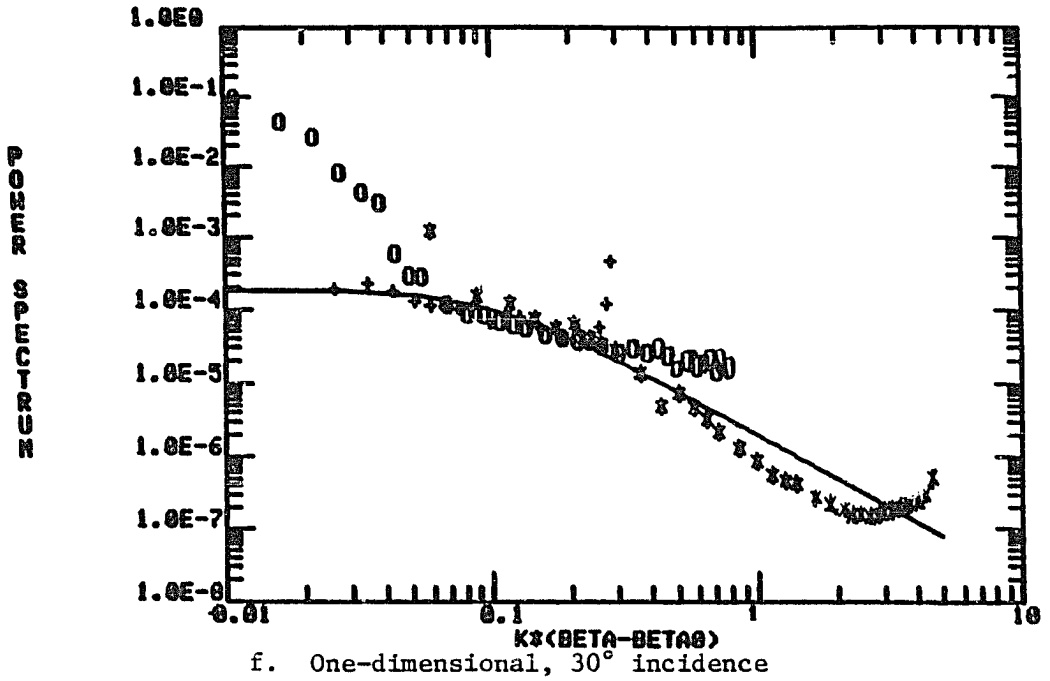

f. One-dimensional, 30° incidence

Fig. 4.8. Power Spectra for Vector Theory and Corresponding Theoretical Curves, for 0.6328 μm, 3.39 μm, and 10.6 μm (Continued).

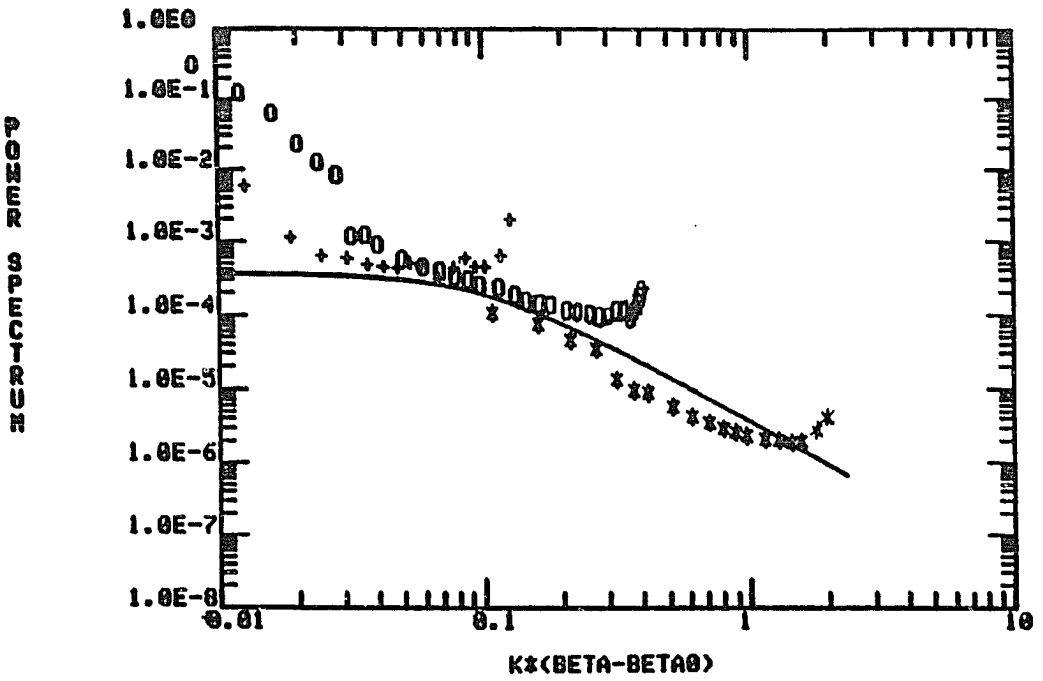

g. One-dimensional, 50° incidence

Fig. 4.8. Power Spectra for Vector Theory and Corresponding Theoretical Curves, for 0.6328 μm, 3.39 μm, and 10.6 μm (Continued).

the real contribution from 3.39-μm light; the top part is clearly the unwanted 10.6-μm CO_2 tail portion. The instrumentation profile for CO_2 at 10.6 μm is smaller than that at 0.035 μm^{-1}. For 3.39-μm and 0.6328-μm radiation, the profiles are smaller than those at 0.85 and 0.1 μm^{-1}, respectively. If we ignore these portions of the profiles, then the spectra of the three wavelengths ranging from 0.01 to 0.1 μm^{-1} coincide well up to 8 μm^{-1} for higher frequencies and to 0.035 μm^{-1} for the lower frequencies. In other words, the whole spectrum covers a range of three decades, provides a unique power spectrum for a single sample, and shows a slope of -2. In addition, as shown in Fig. 4.8c for -10° incidence, some portion of each wavelength's power spectrum that is blocked by the detector can always be filled in by the power spectrum of another wavelength. This is a real physical function and is unique. The spectra of other angles of incidence are presented in Figs. 4.8d through 4.8g. Data for a smaller range of wavelengths (0.4880 to 0.6328 μm) and pp polarizations are shown in Fig. 4.9. Since the wavelengths are so close, the power spectra coincide very well as expected. The feature of this plot is that the power spectra of pp and ss both at 0.6328 μm almost match each other although there is a slight difference in magnitude. It also implies that the spectra of the vector model for different polarizations share the same power spectrum for a single sample. Also shown, in Fig. 4.10, is the power spectrum of uu generated with the uu vector model. It shows the same characteristics as the pp and ss curves. In this case the one-dimensional vector model shows a slope of -2.

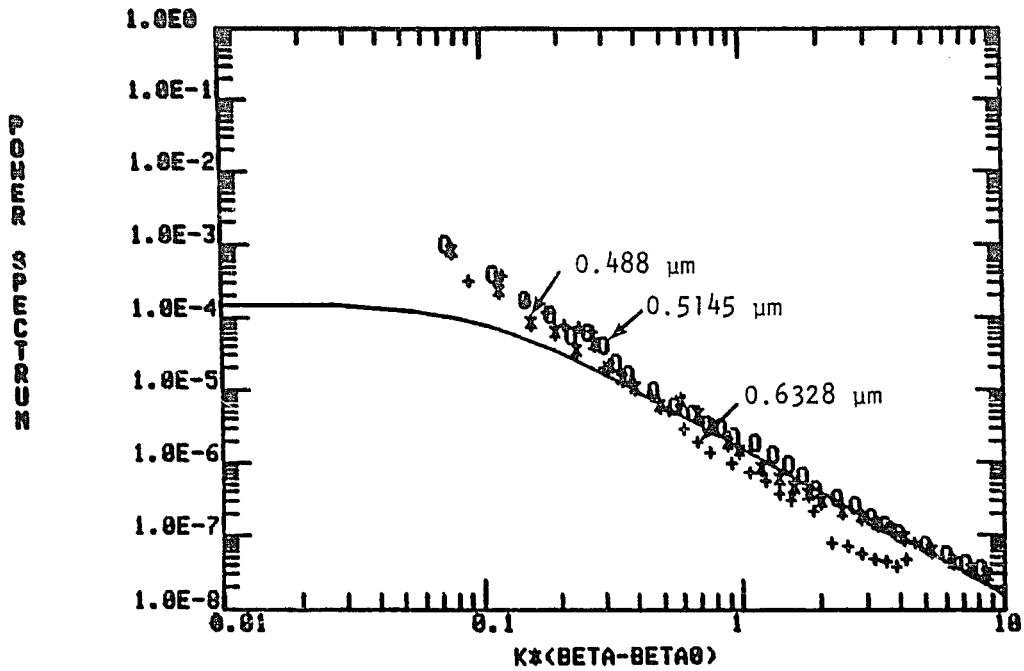

Fig. 4.9. Power Spectrum for Vector Model, pp Polarization, for 0.488 μm, 0.5145 μm, and 0.6328 μm, One-Dimensional, 30° Incidence.

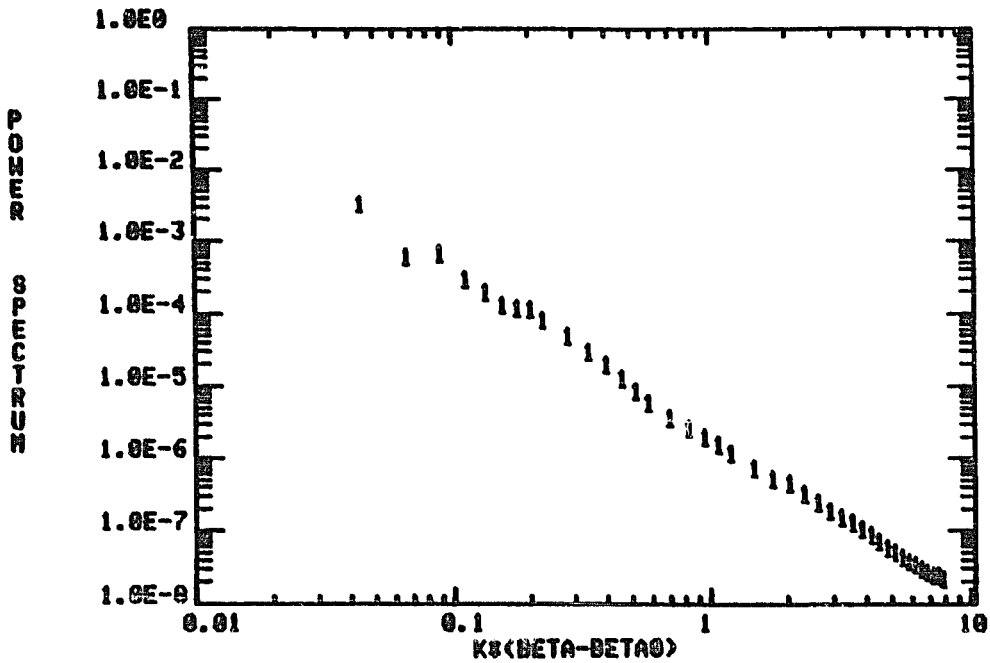

Fig. 4.10. Power Spectrum for Vector Model, uu Polarization, for 0.6328 μm, One-Dimensional, 30° Incidence.

CHAPTER 5

DISCUSSION

In this chapter we discuss the comparisons presented in the previous chapter. Special attention is paid to the various methods of determining optical parameters with BRDF data and the corresponding power spectra of the surface height distribution.

BRDF Curve Fitting

As mentioned in the previous chapter, all experimental curves were fitted with theories by trial and error for values of σ and ℓ. The best-fit value of ℓ for all measurements is 10 μm. As mentioned in Chapter 3, this value can be verified by locating the intersection of two asymptotic curves at 10.6-μm data (see Fig. 4.3b). The agreement is very good.

The best-fit values of σ for all polarizations at different angles of incidence are given with vector theories in Table 5.1. Results of similar curve fitting with a scalar function are summarized in Table 5.2.

Table 5.1 indicates several things. First, in the ss case the rms values fluctuate randomly from 27 Å to 50 Å, with most of the values around 35 Å for all angles of incidence. Second, in the pp case, σ is slightly higher at 10° incidence; and in the uu case, the rms σ value at 30° is the highest. Table 5.1 shows that most of the σ

Table 5.1. Values of rms Surface Height (in Angstroms) for Different Measurements Obtained with Vector Theory.

Angle of incidence	Wavelength, μm		
	0.6328	3.39	10.6
	ss Polarization		
-10°	26.6	40.8	40.8
+10°	26.6	26.6	26.6
-30°	40.8	40.8	40.8
+30°	40.8	40.8	40.8
-50°	26.6	49.6	40.8
+50°	26.6	26.6	26.6
	pp Polarization		
	Wavelength, μm		
	0.6328	0.5145	0.4880
-10°	24.8	24.8	24.8
+10°	24.8	24.8	24.8
-30°	18.8	18.8	18.8
+30°	18.8	18.8	18.8
-50°	13.3	13.3	13.3
+50°	18.8	18.8	18.8
	uu Polarization		
	Wavelength, μm		
	0.6328		
-10°	15.2		
+10°	15.2		
-30°	16.3		
+30°	16.3		
-50°	10.8		
+50°	10.8		

Table 5.2. Values of rms Surface Height (in Angstroms) Obtained by Fitting Scalar Theory to BRDF Data.

Angle of incidence	Wavelength, μm		
	0.6328	3.39	10.6
	ss Polarization		
-10°	8.4	11.9	10
+10°	9.4	8.4	8.4
-30°	10.8	14.8	13.3
+30°	13.3	13.3	11.4
-50°	15.4	16.3	13.3
+50°	16.3	17.8	21.0
	pp Polarization		
-10°	7.7	8.9	9.4
+10°	7.7	8.9	9.4
-30°	8.4	10	9.4
+30°	10	10.8	10.8
-50°	13.3	15.4	16.3
+50°	17.6	16.3	18.1
	uu Polarization		
-10°	7.7		
+10°	5.4		
-30°	7.1		
+30°	7.7		
-50°	10.8		
+50°	10.8		

values drift about some definite value although this value shifts for different polarizations.

The data of Table 5.2 are different from those of Table 5.1. At first glance, the general magnitude of σ is much smaller than that in the previous table. There is a tendency for all σ values to increase almost linearly with respect to the angles of incidence for all directions of polarization and wavelength. Although a few data points (for instance at 3.39 μm and -30° incidence) differ from this trend, they are within experimental error. It appears again as though each angle of incidence sees a different surface for a single sample. Therefore, vector theory, in this respect, yields a more reliable and resonable prediction.

Power Spectrum

Discussion of the power spectrum approach can be divided into two parts. The first is based on the power spectrum generation process, which was discussed earlier. The second is based on theoretical fitting of these power spectra.

We will start from the power spectrum generation process. From a physical point of view, an analytical and measurable quantity must be a continuous, smooth, single-valued function. Consequently, vector theory is far superior to scalar theory. First, the continuity and uniqueness of the vector spectrum (Figs 4.8b and c) are far better than the fragmented and multiple-valued scalar theory and two-dimensional vector model (Fig. 4.6). In addition, the consistency

and coincidence of the power spectrum of uu, pp, and ss indicate that the one-dimensional theory is the most satisfactory.

The second part of this approach concentrates on the curve fitting of the vector power spectrum. The area under the power spectrum is equal to $2\pi\sigma^2$. The power spectra in Figs. 4.8b and c are available only to 0.935 μm^{-1}, and we have no information below this frequency. Nevertheless, we can approximate the area by extrapolating a straight line parallel to the abscissa from 0.035 μm^{-1}. In so doing, we can determine the whole area under the power spectrum and find the value of σ. The results are shown in Table 5.3 together with a one-dimensional Lorentzian model. The continuous lines, as mentioned before, are the one-dimensional Lorentzian model. The agreement between these two models is surprisingly good. One model is derived from experimental measurements with different wavelengths and the other is from fitting with a model that is completely independent of any assumption about the nature of the surface.

The previous two methods of comparison strongly emphasize the superiority of the one-dimensional vector model over all other theories. However, there is one category (Eqs. (2-13) and (2-15)) in which we cannot differentiate one method from the other. The in-plane BRDF measurement for uu polarization agrees with both theories equally well. The results shown in Table 5.4 indicate that the data are close to the theoretical prediction.

Table 5.3. RMS Surface Height (in Angstroms).

Angle of incidence	Area integration of power spectrum (ss)	Curve-fitting on ss power spectrum	Asymptotic area integration of power spectrum
-10°	21.2	28.1	20
+10°	16.7	22.5	18
-30°	23.9	33.5	25.2
+30°	20.1	31.4	24.9
-50°	32.4	35.2	34.5
+50°	32.0	43.1	35.7

Table 5.4. BRDF of uu Polarization of Different Angles of Incidence.

Angle of incidence	BRDF
-10°	1.0
+10°	1.05
-30°	1.3
+30°	1.35
-50°	1.05
+50°	1.25

Additional Method of Measuring σ and ℓ

σ by Asymptotic Method

The integration of the area under the power spectrum for each angle of incidence is tedious and time consuming. The simple technique described in the following paragraphs provides direct information about σ easily.

Because the power spectra of BRDF data have been modeled well by a one-dimensional Lorentzian model, the curve can be represented by two asymptotic lines in the power spectrum plot as shown in Fig. C.1. A detailed calculation of the area under these two lines is given in Appendix C. The result is $2hp_1$, where p_1 is the intersection of these two lines projected on a horizontal axis (in frequency) and h is the highest magnitude of the available power spectra in the lower frequencies. This value is equal to $2\pi\sigma^2$. The rms σ value is thus equal to $(hp_1/\pi)^{1/2}$. The results of each angle of incidence are listed in the fourth column of Table 5.3. They agree well with both the value calculated from the power spectra area integration and the one-dimensional Lorentzian curve-fitting.

Ratio Technique of Calculating ℓ

All the methods used to calculate optical parameters such as σ and ℓ require a knowledge of optical and surface factors. For instance, the BRDF and power-spectrum curve fitting, which yield both σ and ℓ, need both sets of information, and the optical factor has to be known in the power spectrum area integration, which gives σ. However, this ratio technique requires no knowledge of the optical factor.

Basically, two BRDF measurements are necessary at different wavelengths with the same angle of incidence and polarization. A detailed calculation is given in Appendix D, and the results are presented in Table 5.5. Included in Table 5.6 are measurements from mechanical probes (Bennett and Dancy, 1981), optical phase interferometric methods (Koliopoulos, 1981), and all approaches employed previously in this work.

Our data agree excellently although they may depend upon the functional formulation of either an optical factor or surface factor or both. The difference between our data and the interferometric method is tolerable. However, there is a big discrepancy between our work and the mechanical scanning done by Bennett. We are not yet sure of the reason for the discrepancy or which technique is correct.

The last part of this discussion concentrates on the comparisons of the average rms σ predicted by different approaches and various polarizations. Table 5.7 summarizes the results. The first four values are reduced from ss data. They are based on either (1) curve fitting of BRDF data and the corresponding power spectra, or (2) integration of the area under the power spectrum by direct integration or by the asymptotic approach. As seen in Table 5.6, the agreements are good. Similarly, pp and uu rely on the accuracy of their own optical factors.

It appears that the ss theory predicts an rms σ value a few times lower than it should be, which is why the values in the ss case are higher than the rest. Similar arguments are also shared by Bennett (1982).

Table 5.5. Correlation Length from Ratio Technique.

	ℓ (μm)
0.6328 ↔ 3.39 +10°	9.09
3.39 ↔ 10.6 +10°	10.08
0.6328 ↔ 10.6 +10°	9.94
3.39 ↔ 10.6 -10°	8.55
0.6328 ↔ 10.6 -10°	10.74
0.6328 ↔ 3.39 -30°	8.91
Average	9.55

Table 5.6. Correlation Length by Four Methods.

	ℓ (μm)
Average of ℓ by ratio technique	9.55
Asymptotic method at long wavelength	12
Curve-fitting on ss BRDF	10
Curve-fitting on ss power spectrum	10

Table 5.7. Determination of rms Surface Height.

	σ (Å)
Area under ss power spectrum	24.4
Asymptotic area under ss power spectrum	26.4
Curve-fitting of ss BRDF data	32.3
Curve-fitting of ss power spectrum	34.9
Curve-fitting of pp power spectrum	19.9
Curve-fitting of uu power spectrum	14.1
Wyant	8
Bennett	7.5

CHAPTER 6

CONCLUSION

In this study, several scattering theories have been compared, and measurements of highly polished surfaces have been made at five wavelengths from the blue light of an Ar laser to the 10.6-μm radiation of a CO_2 laser. The measured BRDF data and the corresponding power spectra were used to compare the data with vector and scalar theories. In addition, several methods were established to determine the rms surface height and autocorrelation length.

The final conclusions of this work can be stated as follows:

(1) The two-dimensional and one-dimensional scalar models do not agree with our measurements.

(2) The two-dimensional vector model agrees more closely with our measurements but still needs improvement.

(3) The one-dimensional vector model agrees well and shows a slope of -2.

(4) The conclusions are limited to our single sample.

Suggested Future Work

It would be interesting to measure pp polarizations at 3.39 μm and 10.6 μm. The data obtained should facilitate further comparison with scattering theories.

The work to date has concentrated on in-plane geometry because it is easy and convenient to perform. The use of out-of-plane data will broaden our understanding into a three-dimensional framework and will allow verification of comparisons between Eqs. (2.13) and (2.14) of the BRDF relationship. In practice, the out-of-plane study should have wider applications.

BRDF measurements are limited at some small angle by instrumental scattering. Several ways have been proposed (Wolfe, Brooks, and Bartell, 1982) to solve the problem. A second approach to the small-angle problem is to make measurements at longer wavelengths such as 118 μm since frequency p is equal to $(2\pi/\lambda)(\beta-\beta_0)$. Also, improvement of the "no-sample" profile and the long-wavelength performance will provide an understanding of the BRDF at smaller angles for all wavelengths and will extend the power spectrum to smaller frequencies. It will also provide information such as σ directly without relying on the optical factor of the ss theory, which is questionable. Finally, careful calculations and investigation of this theory are essential for predicting a correct rms σ value and magnitude of the BRDF measurement.

A further extension of this work could include the investigation of other samples. Although the work presented in this dissertation established a good relationship between data and the one-dimensional vector theory, the results should be established for other smooth, not-so-smooth, and relatively rough surfaces.

Finally, we have limited the theories and our measurements to thin-film metallic surfaces. Extensions to dielectrics for both reflection and transmission should prove most interesting and rewarding.

APPENDIX A

TRANSITION FROM TWO-DIMENSIONAL TO ONE-DIMENSIONAL MODELS

From Eq. (2.1) the two-dimensional BRDF can be expressed as

$$f_r^{ss} = \text{BRDF} = \frac{1}{\pi^2} k^4 \cdot F_o \cdot W(p). \tag{A.1}$$

The power spectrum W(p) is the Fourier transform of the autocorrelation function $g(\tau)$. If the surface is assumed to be isotropic and the exponential autocorrelation function is also assumed, then the Hankel transform of $g(\tau)$ will yield the result shown in the right-hand side of Eq. (2.1).

For a general case, the explicit form of Eq. (2.1) becomes

$$f_r^{ss} = \frac{1}{\pi^2} k^4 F_o \int_{-\infty}^{\infty} \int_{-\infty}^{\infty} \sigma^2 \exp[-(x,y)/\ell] \exp[-j2\pi(xf_x+yf_y)]\, dxdy, \tag{A.2}$$

where $\exp[-(x,y)/\ell]$ is the two-dimensional exponential autocorrelation function. If it is separable, then $\exp[-(x,y)/\ell]$ is equal to $\exp(-x/\ell) \exp(-y/\ell)$.

Next, we assume the surface is isotropic in the y direction only. We can integrate over $d\phi$ to obtain $dP/d\theta$. We know $d\Omega$ is

$$d\Omega = d\theta_s d\phi_s \sin\theta_s . \tag{A.3}$$

We have $d\phi = 2\pi df_x = (2\pi/\lambda)dk_x = (2\pi/\lambda)\sin\theta_s \cos\phi_s \, d\phi_s$. (A.4)

Substituting Eq. (A.4) into Eq. (A.3) yields

$$d\Omega = \frac{d\theta \sin\theta_s \, d\phi}{(2\pi/\lambda)\sin\theta_s \cos\phi_s} = d\theta \frac{dq}{(2\pi/\lambda)\cos\phi_s} . \tag{A.5}$$

With the assumptions of separability and one-dimensional isotropicity and with Eq. (A.5), $dP/d\theta$ can be obtained by integrating the entire range of q instead of ϕ. Thus Eq. (A.2) becomes

$$\frac{dP}{d\theta} = \frac{16\pi^2}{\lambda^4} [F_o] \frac{\sigma^2}{(2\pi/\lambda)\cos\phi_r} \int_{-\infty}^{\infty} \int_{-\infty}^{\infty} \int_{-\infty}^{\infty} \exp(-x/\ell) \exp(-j2\pi x f_x) \, dx$$

$$\times \exp(-y/\ell) \exp(-j2\pi x f_y) \, dydq . \tag{A.6}$$

But

$$\int_{-\infty}^{\infty} \exp(-x/\ell) \exp(-j2\pi x f_x) \, dx = \frac{2\ell}{1+(2\pi f_x \ell)^2} = \frac{2\ell}{1+(p\ell)^2} \tag{A.7}$$

$$\int_{-\infty}^{\infty} \exp(-y/\ell) \exp(-j2\pi y f_y) \, dy = \frac{2\ell}{1+(2\pi f_y \ell)^2} = \frac{2\ell}{1+(q\ell)^2} \tag{A.8}$$

Equation (A.6) becomes

$$\frac{dP}{d\theta} = \frac{16\pi^2}{\lambda^4}\,[F_o]\,\frac{\sigma^2}{(2\pi/\lambda)\cos\phi_r}\,\frac{2\ell}{1+(p\ell)^2}\int_{-\infty}^{\infty}\frac{2\ell}{1+(q\ell)^2}\,dq\ . \qquad (A.9)$$

However,

$$\int_{-\infty}^{\infty}\frac{2\ell}{1+(q\ell)^2}\,dq = \int\frac{dx}{1+x^2} = \pi\ . \qquad (A.10)$$

Equation (A.9) reduces to

$$\frac{dP}{d\theta} = \frac{16\pi^2}{\lambda^4}\,[F_o]\,\frac{\sigma^2}{(2\pi/\lambda)\cos\phi_s}\,\frac{2\ell}{1+(p\ell)^2}\,2\pi$$

$$= \frac{16\pi^2}{\lambda^3}\,[F_o]\,\frac{1}{\cos\phi_s}\,\frac{2\sigma^2\ell}{1+(p\ell)^2}$$

$$= \frac{16\pi^2}{\lambda^3}\,[F_o]\,\frac{2\sigma^2\ell}{1+(p\ell)^2}\ , \qquad (A.11)$$

where $\cos\phi_s = 1$ for in-plane measurements. Equation (A.11) is exactly the same as Eq. (2.4).

APPENDIX B

COMPARISONS OF VECTOR BRDF THEORIES FOR $\lambda >> \sigma$

Many authors have investigated vector theories. However, only a few have dealt with the case of $\lambda >> \sigma$. The optical factors for their works are listed in Tables B.1 to B.4 for pp, ps, sp, and ss polarizations. All the factors can be applied to metals and dielectrics except those by Marvin et al. (1975), which are for metals only. An error occurs in the pp polarization of Maradudin and Mills (1975). It is caused by inadequate boundary conditions, which are discussed by Marvin et al. An additional point is that there is an ambiguity among them. For two quantities A and B, the equality $|A|\cdot|B| \geq |AB|$ exists if and only if both are real. This type of inequality occurred, for instance, both in Maradudin and Mills and in Church et al. (1977) because the dielectric constant for a dielectric material is generally complex for most of the spectrum.

The comparisons presented here concentrate on the factors by Marvin et al. and the rest. We attempt to prove that, under certain circumstances, the factors by all the groups are the same except for the above ambiguity. Thus we select Marvin et al. and Church et al. for our comparison. We start with pp polarization and continue on to the ps, sp, and ss cases.

Table B.1. Optical Factors for pp Polarization ($\lambda >> \sigma$).

Authors	Optical factors
Maradudin and Mills (1975)[a,b]	$\lvert\varepsilon(\omega)-1\rvert^2 \dfrac{\lvert\cos\phi_s[\varepsilon(\omega)-\sin^2\theta_s]^{1/2}[\varepsilon(\omega)-\sin\theta_i{}^2]^{1/2} - \frac{1}{2}\sin\theta_i\sin\theta_s[\varepsilon^2(\omega)+1]\rvert^2}{\lvert\varepsilon(\omega)\cos\theta_s + [\varepsilon(\omega)-\sin^2\theta_s]^{1/2}\rvert^2\lvert\varepsilon(\omega)\cos\theta_i + [\varepsilon(\omega)-\sin^2\theta_i]^{1/2}\rvert^2}$
Marvin, Toigo, and Celli (1975)[c]	$\dfrac{[(\sin^2\theta_i-\varepsilon)^{1/2}(\sin^2\theta_s-\varepsilon)^{1/2}\cos\phi + \varepsilon\sin\theta_i\sin\theta_s]^2}{[(\sin\theta_i-\varepsilon\cos^2\theta_i)(\sin^2\theta_s-\varepsilon\cos^2\theta_s)]}$
Church, Jenkinson, and Zavada (1977)	$\lvert\varepsilon-1\rvert^2 \left\lvert \dfrac{\sqrt{\varepsilon-\sin^2\theta_i}\,\sqrt{\varepsilon-\sin^2\theta_s}\,\cos\phi_s - \varepsilon\sin\theta_i\sin\theta_s}{(\varepsilon\cos\theta_i + \sqrt{\varepsilon-\sin^2\theta_i})(\varepsilon\cos\theta_s + \sqrt{\varepsilon-\sin^2\theta_s})} \right\rvert^2$
Ishimaru (1978)[d]	$\left\lvert \dfrac{(\varepsilon_r-1)[\varepsilon_r\sin\theta_i\sin\theta_s - \cos\phi_s(\varepsilon_r-\sin^2\theta_i)^{1/2}(\varepsilon_r-\sin^2\theta_s)^{1/2}]}{[\varepsilon_r\cos\theta_i + (\varepsilon_r-\sin^2\theta_i)^{1/2}][\varepsilon_r\cos\theta_s + (\varepsilon_r-\sin^2\theta_s)^{1/2}]} \right\rvert^2$
Barrick and Peake (1967)	$\left\lvert \dfrac{(\varepsilon_r-1)[\varepsilon_r\sin\theta_i\sin\theta_s - \cos\phi_s\sqrt{\varepsilon_r\mu_r-\sin^2\theta_i}\,\sqrt{\varepsilon_r\mu_r-\sin^2\theta_s}\,] + \varepsilon_r{}^2(\mu_r-1)\cos\phi_s}{[\varepsilon_r\cos\theta_i + (\varepsilon_r-\sin^2\theta_i)^{1/2}][\varepsilon_r\cos\theta_s + (\varepsilon_r-\sin^2\theta_s)^{1/2}]} \right\rvert^2$

[a] A difference of $|A||B| \neq |AB|$ exists between this expression and those of Church et al. (1977), Ishimaru (1978), and Barrick and Peake (1967).

[b] $\frac{1}{2}\sin\theta_i\sin\theta_s[\varepsilon^2(\omega)+1]$ is $\sin\theta_i\sin\theta_s\varepsilon(\omega)$ corrected by Marvin et al. (1975). It is caused by inadequate boundary conditions.

[c] ε = dielectric constant.

[d] Follow Barrick and Peake (1967); set $\mu_r = 1$; ε_r = dielectric constant.

Table B.2. Optical Factors for ps Polarization ($\lambda >> \sigma$).

Authors	Optical factors
Maradudin and Mills (1975)[a]	$\sin^2\phi_s \lvert\varepsilon(\omega)-1\rvert^2 \dfrac{\lvert\varepsilon(\omega)-\sin^2\theta_i\rvert}{\lvert\cos\theta_s+[\varepsilon(\omega)-\sin^2\theta_s]^{1/2}\rvert^2 \lvert\varepsilon(\omega)\cos\theta_i+[\varepsilon(\omega)-\sin^2\theta_i]^{1/2}\rvert^2}$
Marvin, Toigo, and Celli (1975)	$\sin^2\phi_s \dfrac{\sin^2\theta_i-\varepsilon}{\sin^2\theta_i-\varepsilon\cos^2\theta_i}$
Church, Jenkinson, and Zavada (1977)	$\lvert\varepsilon-1\rvert^2 \left\lvert \dfrac{\sqrt{\varepsilon-\sin^2\theta_i}\,\sin\phi_s}{(\varepsilon\cos\theta_i+\sqrt{\varepsilon-\sin^2\theta_i})\,(\cos\theta_s+\sqrt{\varepsilon-\sin^2\theta_s})} \right\rvert^2$
Ishimaru (1978)	$\left\lvert \dfrac{(\varepsilon_r-1)(\varepsilon_r-\sin^2\theta_s)^{1/2}\sin\phi_s}{[\cos\theta_i+(\varepsilon_r-\sin^2\theta_i)^{1/2}]\,[\varepsilon_r\cos\theta_s+(\varepsilon_r-\sin^2\theta_s)^{1/2}]} \right\rvert^2$
Barrick and Peake (1967)	$\left\lvert \sin\phi_s \dfrac{\varepsilon_r(\mu_r-1)\sqrt{\varepsilon_r\mu_r-\sin^2\theta_i}-\mu_r(\varepsilon_r-1)\sqrt{\varepsilon_r\mu_r-\sin^2\theta_s}}{[\mu_r\cos\theta_i+\sqrt{\varepsilon_r\mu_r-\sin^2\theta_i}\,]\,[\varepsilon_r\cos\theta_s+\sqrt{\varepsilon_r\mu_r-\sin^2\theta_s}\,]} \right\rvert^2$

[a] A difference of $|A||B| \neq |AB|$ exists between this expression and those of Church et al. (1977), Ishimaru (1978), and Barrick and Peake (1967).

Table B.3. Optical Factors for sp Polarization ($\lambda >> \sigma$).

Authors	Optical factors
Maradudin and Mills (1975)[a]	$\sin^2\phi_s \dfrac{\lvert\varepsilon(\omega)-\sin^2\theta_s\rvert \; \lvert\varepsilon(\omega)-1\rvert^2}{\lvert\varepsilon(\omega)\cos\theta_s + [\varepsilon(\omega)-\sin^2\theta_s]^{1/2}\rvert^2 \; \lvert\cos\theta_i + [\varepsilon(\omega)-\sin^2\theta_i]^{1/2}\rvert^2}$
Marvin, Toigo, and Celli (1975)	$\sin^2\phi_s \dfrac{\sin^2\theta_s - \varepsilon}{\sin^2\theta_s - \varepsilon\cos^2\theta_s}$
Church, Jenkinson, and Zavada (1977)	$\lvert\varepsilon-1\rvert^2 \left\lvert \dfrac{\sqrt{\varepsilon-\sin^2\theta_s}\,\sin\phi_s}{(\cos\theta_i + \sqrt{\varepsilon-\sin^2\theta_i})\,(\varepsilon\cos\theta_s + \sqrt{\varepsilon-\sin^2\theta_s})} \right\rvert^2$
Ishimaru (1978)	$\left\lvert \dfrac{\sin\phi_s(\varepsilon_r-1)(\varepsilon_r-\sin^2\theta_i)^{1/2}}{[\varepsilon_r\cos\theta_i + (\varepsilon_r-\sin^2\theta_i)^{1/2}][\cos\theta_s + (\varepsilon_r-\sin^2\theta_s)^{1/2}]} \right\rvert^2$
Barrick and Peake (1967)	$\sin\phi_s \dfrac{\mu_r(\varepsilon_r-1)\sqrt{\varepsilon_r\mu_r-\sin^2\theta_i} - \varepsilon_r(\mu_r-1)\sqrt{\varepsilon_r\mu_r-\sin^2\theta_s}}{[\varepsilon_r\cos\theta_i + \sqrt{\varepsilon_r\mu_r-\sin^2\theta_i}\,][\mu_r\cos\theta_s + \sqrt{\varepsilon_r\mu_r-\sin^2\theta_s}\,]}$

[a] A difference of $\lvert A\rvert\lvert B\rvert \neq \lvert AB\rvert$ exists between this expression and those of Church et al. (1977), Ishimaru (1978), and Barrick and Peake (1967).

Table B.4. Optical Factors for ss Polarization ($\lambda >> \sigma$).

Authors	Optical factors
Maradudin and Mills (1975)[a]	$\cos^2\phi_s \dfrac{\lvert\varepsilon(\omega)-1\rvert^2}{\lvert\cos\theta_s + [\varepsilon(\omega)-\sin^2\theta_s]^{1/2}\rvert^2 \lvert\cos\theta_i + [\varepsilon(\omega)-\sin^2\theta_i]^{1/2}\rvert^2}$
Marvin, Toigo, and Celli (1975)	$\cos^2\phi_s$
Church, Jenkinson, and Zavada (1977)	$\lvert\varepsilon-1\rvert^2 \left\lvert \dfrac{\cos\phi_s}{(\cos\theta_i + \sqrt{\varepsilon-\sin^2\theta_i})(\cos\theta_s + \sqrt{\varepsilon-\sin^2\theta_s})} \right\rvert^2$
Ishimaru (1978)	$\left\lvert \dfrac{(\varepsilon_r-1)\cos\phi_s}{[\cos\theta_i + (\varepsilon_r-\sin^2\theta_i)^{1/2}][\cos\theta_s + (\varepsilon_r-\sin^2\theta_s)^{1/2}]} \right\rvert^2$
Barrick and Peake (1967)	$\left\lvert \dfrac{[(\mu_r-1)(\mu_r\sin\theta_i\sin\theta_s - \cos\phi_s\sqrt{\varepsilon_r\mu_r-\sin^2\theta_i}\,\sqrt{\varepsilon_r\mu_r-\sin^2\theta_s} + \mu_r^2(\varepsilon_r-1)\cos\phi_s]}{[\mu_r\cos\theta_i + \sqrt{\varepsilon_r\mu_r-\sin^2\theta_i}\,][\mu_r\cos\theta_s + \sqrt{\varepsilon_r\mu_r-\sin^2\theta_s}\,]} \right\rvert^2$

[a] A difference of $|A||B| \neq |AB|$ exists between this expression and those of Church et al. (1977), Ishimaru (1978), and Barrick and Peake (1967).

pp Polarization

In the case of metal, the dielectric constant is large and negative, i.e., $-|\varepsilon| > 0$, and also the real part is much larger than the imaginary part. The first two quantities in the numerator of Church et al. become:

$$(\varepsilon - \sin^2\theta_i)^{\frac{1}{2}}(\varepsilon - \sin^2\theta_s)^{\frac{1}{2}} = [i(\sin^2\theta_i - \varepsilon)^{\frac{1}{2}}][i(\sin^2\theta_s - \varepsilon)^{\frac{1}{2}}]$$

$$= -(\sin^2\theta_i - \varepsilon)^{\frac{1}{2}}(\sin^2\theta_s - \varepsilon)^{\frac{1}{2}}. \quad \text{(B.1)}$$

The numerator now can be rearranged as

$$|\sqrt{\varepsilon-\sin^2\theta_i}\ \sqrt{\varepsilon-\sin^2\theta_s}\ \cos\phi_s - \varepsilon \sin\theta_i \sin\theta_s|^2$$

$$= |-(\sin^2\theta_i-\varepsilon)^{1/2}(\sin^2\theta_s-\varepsilon)^{1/2}\ \cos\phi_s - \varepsilon \sin\theta_i \sin\theta_s|^2$$

$$= |(\sin^2\theta_i-\varepsilon)^{1/2}(\sin^2\theta_s-\varepsilon)^{1/2}\ \cos\phi_s + \varepsilon \sin\theta_i \sin\theta_s|^2. \quad \text{(B.2)}$$

Equation (B.2) is exactly the same as the numerator of Marvin et al. Similarly the denominator of Church et al. can be simplified as follows:

$$|(\varepsilon \cos\theta_i + \sqrt{\varepsilon-\sin^2\theta_i})\ (\varepsilon \cos\theta_s + \sqrt{\varepsilon-\sin^2\theta_s})|^2$$

$$= \left|\left[\varepsilon \cos\theta_i + i(\sin^2\theta_i-\varepsilon)^{1/2}\right]\left[\varepsilon \cos\theta_s + i(\sin^2\theta_s-\varepsilon)^{1/2}\right]\right|^2$$

$$= |\{\varepsilon^2 \cos\theta_i \cos\theta_s - (\sin^2\theta_i-\varepsilon)^{1/2}(\sin^2\theta_s-\varepsilon)^{1/2}\}$$

$$+ i\{\varepsilon \cos\theta_s(\sin^2\theta_i-\varepsilon)^{1/2} + \varepsilon \cos\theta_i(\sin^2\theta_s - \varepsilon)^{1/2}\}|^2$$

$$= \{\varepsilon^2 \cos\theta_i \cos\theta_s - (\sin^2\theta_i-\varepsilon)^{1/2}(\sin^2\theta_s-\varepsilon)^{1/2}\}^2$$

$$+ \{\varepsilon \cos\theta_s(\sin^2\theta_i-\varepsilon)^{1/2} + \varepsilon \cos\theta_i(\sin^2\theta_s-\varepsilon)^{1/2}\}^2$$

$$= \varepsilon^4 \cos^2\theta_i \cos^2\theta_s + (\sin^2\theta_i-\varepsilon)(\sin^2\theta_s-\varepsilon)$$

$$- 2\varepsilon^2 \cos\theta_i \cos\theta_s(\sin^2\theta_i-\varepsilon)^{1/2}(\sin\theta_s-\varepsilon)^{1/2}$$

$$+ \varepsilon^2 \cos^2\theta_s(\sin^2\theta_i-\varepsilon) + \varepsilon^2 \cos^2\theta_i(\sin^2\theta_s-\varepsilon)$$

$$+ 2\varepsilon^2 \cos\theta_i \cos\theta_s(\sin^2\theta_i-\varepsilon)^{1/2}(\sin\theta_s-\varepsilon)^{1/2}$$

$$= \varepsilon^2 \cos^2\theta_i(\varepsilon^2\cos^2\theta_s+\sin^2\theta_s-\varepsilon)$$

$$+ (\sin^2\theta_i-\varepsilon)(\varepsilon^2 \cos^2\theta_s+\sin^2\theta_s-\varepsilon)$$

$$= (\varepsilon^2 \cos^2\theta_s+\sin^2\theta_s-\varepsilon)(\varepsilon^2 \cos^2\theta_i+\sin^2\theta_i-\varepsilon)$$

$$= (\varepsilon-1)^2(\sin^2\theta_s-\varepsilon \cos^2\theta_s)(\sin^2\theta_i-\varepsilon \cos^2\theta_i) . \qquad (B.3)$$

The first term $(\varepsilon-1)^2$ automatically cancels with $|\varepsilon-1|^2$ in Church et al. The rest is equal to the denominator of Marvin et al.

ps Polarization

The numerator has been compared for the pp case. What is left is the denominator:

$$|(\varepsilon \cos\theta_i + \sqrt{\varepsilon-\sin^2\theta_i})(\cos\theta_s + \sqrt{\varepsilon-\sin^2\theta_s})|^2$$

$$= |(\varepsilon \cos\theta_i + i\sqrt{\sin^2\theta_i-\varepsilon})(\cos\theta_s + i\sqrt{\sin^2\theta_s-\varepsilon})|^2$$

$$= |\{\varepsilon \cos\theta_i \cos\theta_s - [(\sin\theta_i-\varepsilon)(\sin^2\theta_s-\varepsilon)]^{1/2}\}$$

$$+ i\{\cos\theta_s(\sin^2\theta_i-\varepsilon)^{1/2} + \varepsilon \cos\theta_i(\sin^2\theta_s-\varepsilon)^{1/2}\}|^2$$

$$= \{\varepsilon \cos\theta_i \cos\theta_s - [(\sin\theta_i-\varepsilon)(\sin^2\theta_s-\varepsilon)]^{1/2}\}^2$$

$$+ \{\cos\theta_s(\sin^2\theta_i-\varepsilon)^{1/2} + \varepsilon \cos\theta_i(\sin^2\theta_s-\varepsilon)^{1/2}\}^2$$

$$= c^2 \cos^2\theta_i \cos^2\theta_s + (\sin^2\theta_i-\varepsilon)(\sin^2\theta_s-\varepsilon)$$

$$- 2\varepsilon \cos\theta_i \cos\theta_s(\sin^2\theta_i-\varepsilon)^{1/2}(\sin^2\theta_s-\varepsilon)^{1/2}$$

$$+ \cos^2\theta_s(\sin^2\theta_i-\varepsilon) + \varepsilon^2 \cos\theta_i(\sin^2\theta_s-\varepsilon)$$

$$+ 2\varepsilon \cos\theta_i \cos\theta_s(\sin^2\theta_i-\varepsilon)^{1/2}(\sin^2\theta_s-\varepsilon)^{1/2}$$

$$= \varepsilon^2 \cos^2\theta_i[\cos^2\theta_s+\sin^2\theta_s-\varepsilon] + (\sin^2\theta_i-\varepsilon)[\cos^2\theta_s+\sin\theta_s+\varepsilon]$$

$$= \varepsilon^2 \cos^2\theta_i[1-\varepsilon] + (\sin^2\theta_i-\varepsilon)[1+\varepsilon]$$

$$= (\varepsilon^2 \cos^2\theta_i + \sin^2\theta_i - \varepsilon)(1 - \varepsilon)$$

$$= (\sin^2\theta_i - \varepsilon \cos^2\theta_i)(1 - \varepsilon)^2 \ . \qquad \text{(B.4)}$$

The first quantity is the same as that in Marvin et al., and the second term cancels out automatically with $|\varepsilon-1|^2$ in Church et al.

sp Polarization

This polarization is very similar to that of the ps case. If we interchange i with s and vice versa, the calculation is exactly the same as for the ps case.

ss Polarization

If we can prove for the case of metal that the optical factor of Church et al. is equal to $(\varepsilon-1)^2$, then the $|\varepsilon-1|^2$ in that group can be canceled:

$$|[(\cos\theta_s + (\varepsilon-\sin^2\theta_s)^{1/2}][\cos\theta_i + (\varepsilon-\sin^2\theta_i)^{1/2}]\ |^2$$

$$= |[\cos\theta_s + i(\sin^2\theta_s-\varepsilon)^{1/2}][\cos\theta_i + i(\sin^2\theta_i-\varepsilon)^{1/2}\ ]\ |^2$$

$$= \left| \{\cos\theta_s \cos\theta_i - [(\sin^2\theta_s-\varepsilon)(\sin^2\theta_i-\varepsilon)]^{1/2}\} \right.$$

$$\left. + i[(\sin^2\theta_i-\varepsilon)^{1/2} \cos\theta_s + (\sin^2\theta_s-\varepsilon)^{1/2} \cos\theta_i] \right|^2$$

$$= \{\cos\theta_s \cos\theta_i - [(\sin^2\theta_s-\varepsilon)(\sin^2\theta_i-\varepsilon)]^{1/2}\}^2$$

$$+ [(\sin^2\theta_i-\varepsilon)^{1/2} \cos\theta_s + (\sin^2\theta_s-\varepsilon)^{1/2} \cos\theta_i]^2$$

$$= \cos^2\theta_s \cos^2\theta_i + [(\sin^2\theta_s-\varepsilon)(\sin^2\theta_i-\varepsilon)]$$

$$- 2 \cos\theta_s \cos\theta_i(\sin^2\theta_s-\varepsilon)^{1/2}(\sin_i{}^2\theta-\varepsilon)^{1/2}$$

$$+ (\sin^2\theta_i-\varepsilon)(\cos^2\theta_s + (\sin^2\theta_s-\varepsilon) \cos^2\theta_i$$

$$+ 2 \cos\theta_s \cos\theta_i(\sin^2\theta_s-\varepsilon)^{1/2}(\sin_i{}^2\theta-\varepsilon)^{1/2}$$

$$= \cos^2\theta_i \cos^2\theta_i + \sin^2\theta_s \sin^2\theta_i + \varepsilon^2$$

$$- \varepsilon(\sin^2\theta_i+\sin^2\theta_s) + \sin^2\theta_i \cos^2\theta_s$$

$$+ \sin^2\theta_s \cos^2\theta_i - \varepsilon(\cos^2\theta_s + \cos^2\theta_i)$$

$$= \cos^2\theta_s(\cos^2\theta_i + \sin^2\theta_i)$$

$$+ \sin^2\theta_s(\sin^2\theta_i+\cos^2\theta_i) + \varepsilon^2 - \varepsilon(\sin^2\theta_i+\cos^2\theta_i)$$

$$- \varepsilon(\cos^2\theta_s + \sin^2\theta_s)$$

$$= (\cos^2\theta_s + \sin^2\theta_s) + \varepsilon^2 - 2\varepsilon$$

$$= (1-\varepsilon)^2 \,. \qquad \text{(B.5)}$$

APPENDIX C

ASYMPTOTIC INTEGRATION

When the surface spectrum can be represented by two straight lines on a log-log plot (Fig. C.1), the integration is relatively simple. The area under the curve is given by

$$A = \int_0^{p_1} h \, dp + \int_{p_1}^{p_2} \frac{K}{p^m} \, dp \qquad (C.1)$$

where

K = constant

m = 2 or 3.

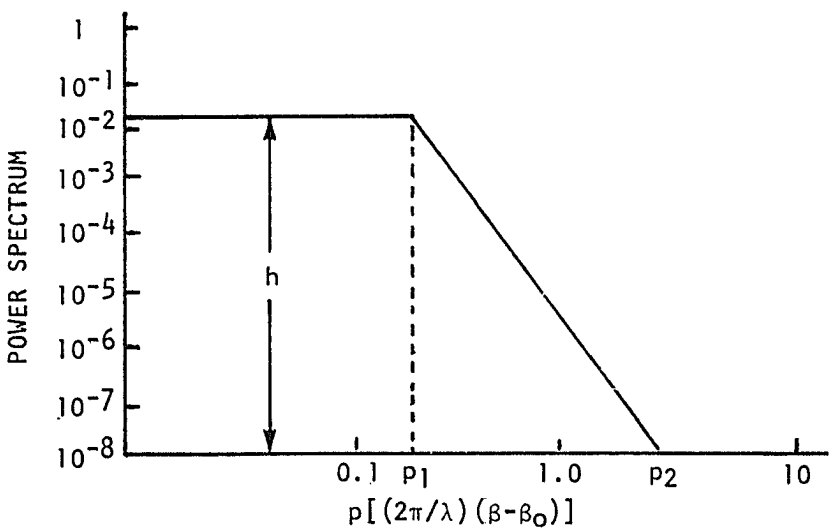

Fig. C.1. Log-Log Plot of Asymptotic Curve of Power Spectrum.

This reduces to

$$A_1 = hp_1 + K(1/p_1 - 1/p_2) \tag{C.2}$$

$$A_2 = hp_1 + K(1/p_1^2 - 1/p_2^2) . \tag{C.3}$$

For most cases (all cases we have considered), p_2 is much greater than p_1 and the second term in the parentheses may be ignored. At the intersection point,

$$h = K/p_1^2 \quad \text{or} \quad h = K/p_1^3 \tag{C.4}$$

$$hp_1 = K/p_1 \quad \text{or} \quad hp_1 = K/p_1^2 . \tag{C.5}$$

Thus the two areas reduce to

$$A_1 = 2\,hp_1 \tag{C.6}$$

$$A_2 = 1.5\,hp_1 . \tag{C.7}$$

These areas are equal to $2\pi\sigma^2$, so

$$\sigma_1 = (hp_1/\pi)^{1/2} \tag{C.8}$$

$$\sigma_2 = (3hp_1/4\pi)^{1/2} . \tag{C.9}$$

APPENDIX D

RATIO TECHNIQUE FOR CALCULATING ℓ

We assume that BRDF measurements have been made at each of two wavelengths. Then

$$f_{r_1} = \frac{2}{\pi} k_1^2 F_o 2\sigma^2 \ell / [1 + k_1^2 (\beta - \beta_o)^2 \ell^2] \tag{D.1}$$

$$f_{r_2} = \frac{2}{\pi} k_2^3 F_o 2\sigma^2 \ell / [1 + k_2^3 (\beta - \beta_o)^2 \ell^2]. \tag{D.2}$$

The ratio R is then found to be

$$R = \frac{\lambda_2}{\lambda_1}^3 \frac{[1 + k_2^2 (\beta - \beta_o)^2 \ell^2]}{[1 + k_1^2 (\beta - \beta_o)^2 \ell^2]} . \tag{D.3}$$

Let $R_\lambda = \lambda_2 / \lambda_1$. Then

$$\frac{R}{R_\lambda^3} [1 + k_1^2 (\beta - \beta_o)^2] = [1 + k_2^2 (\beta - \beta_o)^2] \tag{D.4}$$

$$\frac{R}{R_\lambda^3} - 1 = (2\pi)^2 (\beta - \beta_o)^2 [(1/\lambda_2)^2 - (1/\lambda_1)^2] \ell^2 \tag{D.5}$$

$$\ell^2 = \frac{(R/R_\lambda^3 - 1)(\lambda_1^2 - \lambda_2^2)}{[2\pi(\beta - \beta_o)]^2 (\lambda_1^2 - \lambda_2^2)} . \tag{D.6}$$

Although further manipulation is possible, the solution for ℓ is apparent. It is given in terms of the two known wavelengths and the value of $\beta-\beta_o$. A similar result is obtainable for the two-dimensional case.

REFERENCES

Barrick, D. E., and W. E. Peake, "Scattering from surfaces with different roughness scales: analysis and interpretation," Technical Report AD662751, Battelle Memorial Institute (1967).

Bartell, F. O., E. L. Dereniak, and W. L. Wolfe, SPIE 257, 154 (1980).

Beaglehole, D., and O. Hunderi, Phys. Rev. B 2, 309 (1970).

Beckmann, P., and A. Spizzichino, The Scattering of Electromagnetic Waves from Rough Surface (Pergamon, New York, 1963).

Bennett, J. M., Appl. Opt. 15, 2705 (1976).

Bennett, J. M. (Naval Weapons Center, China Lake, Cal.), personal communication (1982).

Bennett, J. M., and J. H. Dancy, Appl. Opt. 20, 1785 (1981).

Brooks, L. D., Ph.D. dissertation, University of Arizona, Tucson, Arizona (1982).

Chandley, P. J., Opt. Quantum Electron. 8, 323 (1976).

Chandley, P. J., Opt. Quantum Electron. 11, 413 (1979).

Chandley, P. J., and W. T. Welford, Opt. Quantum Electron. 7, 393 (1975).

Church, E. L., H. A. Jenkinson, and J. M. Zavada, Opt. Eng. 16, 360 (1977).

Davies, H., Proc. IEE 101, 209 (1954).

Eastman, J., and P. W. Baumeister, Opt. Commun. 12, 418 (1974).

Elson, J. M., and J. M. Bennett, J. Opt. Soc. Am. 69, 31 (1979a).

Elson, J. M., and J. M. Bennett, Opt. Eng. 18, 116 (1979b).

Fung, A. K., and H. Chang, IEEE Trans. Antennas Propag. AP-17, 590 (1969).

Harvey, J. E., Ph.D. Dissertation, University of Arizona, Tucson, Arizona (1976).

Ishimaru, A., Wave Propagation and Scattering in Random Media (Academic Press, New York, 1978).

Koliopoulos, C., Ph.D. Dissertation, University of Arizona, Tucson, Arizona (1981).

Kroger, E., and E. Kretschmann, Z. Phys. 237, 1 (1970).

Leader, J. C., J. Appl. Phys. 42, 4808 (1971).

Marvin, A., F. Toigo, and V. Celli, Phys. Rev. B 11, 2777 (1975).

Maradudin, A. A., and D. L. Mills, Phys. Rev. B 11, 1392 (1975).

Nicodemus, F., Appl. Opt. 9, 1474 (1970).

Noll, R. J., and P. Glenn, Appl. Opt. 21, 1824 (1982).

Rayleigh, Lord, The Theory of Sound, Vol. 2 (Dover, New York, 1945).

Rice, S. O., Commun. Pure and Appl. Math. 4, 351 (1951).

Silver, S., Microwave Antenna Theory and Design (McGraw-Hill, New York, 1947), p. 161.

Wang, Y., and W. L. Wolfe, "A comparison of theory and experiment for scattering from microrough surfaces," J. Opt. Soc. Am. (submitted, 1983).

Wolfe, W. L, L. D. Brooks, and F. O. Bartell, "Description and limitations of an automated scatterometer," Proc. SPIE 362 (submitted, 1982).

Young, R. P., Proc. SPIE 65, 57 (1975).